

Homogenization of the vibro–acoustic transmission on periodically perforated elastic plates with arrays of resonators

E. Rohan^{a,*}, V. Lukeš^a

^a*European Centre of Excellence, NTIS New Technologies for Information Society, Faculty of Applied Sciences,
University of West Bohemia,
Univerzitní 22, 30614 Plzeň, Czech Republic*

Abstract

Based on our previous work, we propose a homogenized model of acoustic waves propagating through periodically perforated elastic plates with metamaterial properties due to embedded arrays of soft elastic inclusions serving for resonators. Such structures enable to suppress the acoustic transmission for selected frequency bands. Homogenization of the vibro-acoustic fluid-structure interaction problem in a 3D complex geometry of the transmission layer leads to effective transmission conditions prescribed on the acoustic metasurface associated with the mid-plane of the Reissner-Mindlin plate. Asymptotic analysis with respect to the layer thickness, proportional to the plate thickness and to the perforation period, yields an implicit Dirichlet-to-Neumann operator defined on the homogenized metasurface. An efficient method is proposed for computing frequency-dependent effective parameters involved in the homogenized model of the layer. These can change their signs, thus modifying the acoustic impedance and the effective mass of the metasurface. The global problem of the acoustic wave propagation in a waveguide fitted with the plate is solved using the finite element method. The homogenized interface allows for a significant reduction of the computational model. Numerical illustrations are presented.

Keywords: Vibro-acoustic transmission, perforated plate, acoustic metasurface, acoustic metamaterial, two scale homogenization, Helmholtz equation, finite element method, spectral decomposition

1. Introduction

Absorption of acoustic waves using acoustic metasurfaces belongs to challenging and interesting issues from both the scientific and engineering points of view. Many structures (engine casing) and devices incorporate perforated plates, or panels which enable for fluid transport, and simultaneously should reduce the noise transmission and emission due to the structure vibration. In general, acoustic absorption is achieved by means of porous

*Corresponding author

Email addresses: rohan@kme.zcu.cz (E. Rohan), vlukes@kme.zcu.cz (V. Lukeš)

and fibrous materials, or micro-perforated panels. Such structures are relatively very thick to achieve required absorption. Recently some tunable structures, like space-coiling structures provide absorbing design solutions with reduced thickness. We omit approaches based on active absorption which require expensive sophisticated electrical control. Even passive behaviour of metasurfaces constituted by elastic composite materials with periodic arrangement of constituents can exhibit special effective acoustic impedance which admits permeable but also sound-resistant structure ensuring reduced noise radiation. In many devices, or constructions, both these mutually contradictory properties are required to ensure functionality and environmental feasibility at the same time. While the former requirement is often related to device functionality, admitting air flow through the perforations (*e.g.* cooling by ventilation), the latter one is obvious but nontrivial to achieve – besides reducing undesired noise radiation, also suppressing the panel vibrations which may be induced by incident acoustic wave, or independently by structural vibrations induced the device (engines, mechanic transmissions *etc.*).

The aim of the present paper is to present a homogenized interface model of the vibro-acoustic transmission through a metasurface designed as a perforated elastic plate with resonators. We derive transmission conditions on the homogenized interface replacing the problem of the fluid-structure interaction in a very complex geometry. As the advantage, such a homogenized interface reduces significantly the related numerical discretized model and, thereby, the computational complexity when compared to the direct numerical simulations which consist in solving directly the vibro-acoustic problem with a 3D elastic structure describing the panel, *cf.* [1]. Although the homogenization approach is not completely new in the context of the acoustic transmission, it has not been applied so far to elastic plates with resonators represented by strong heterogeneities in the elasticity coefficients.

The homogenization strategy has been applied in situations when thin rigid perforated plate represented by interface Γ_0 is characterized by the thickness $\approx \delta$ proportional to the size of the perforating holes $\varepsilon \approx \delta$. It has been shown [2, 3] that the homogenized interface is totally transparent for the acoustic field at the zero order $o(\varepsilon^0)$ terms of the model which describes the limit behaviour for $\varepsilon \rightarrow 0$, *cf.* [4]. To get a nontrivial model which captures acoustic impedance of the thin interface, a higher order approximation involving the correctors at order $o(\varepsilon^1)$ must be considered. A slightly different treatment of the interface homogenization is based on the so-called inner and outer asymptotic expansions, see *e.g.* [5, 6, 7]. In contrast with [2] dealing with thin perforated interfaces only, in our previous studies [8, 9] we were concerned with homogenization of a fictitious layer containing the perforated plate. Nonlocal transmission conditions were obtained as the two-scale homogenization limit $\varepsilon \rightarrow 0$ of the acoustic field interacting with the rigid, or elastic plate with an approximation respecting a given finite scale $\varepsilon_0 > 0$.

Acoustic metasurfaces [10, 11, 12, 13] and their efficient modelling is the second issue of the present paper. The area of electromagnetic wave propagation in periodic structures equipped with resonators and the design of photonic crystals provided inspirations how to manipulate the elastic waves in solids and fluids. However, there are remarkable differences between the two types of waves due to different physical phenomena. The so-called

Bragg scattering of electromagnetic waves which arises from the diffraction and refraction of incident waves in a crystalline structure whose the periodicity is comparable to the wave length, the same phenomenon in the acoustics would require large structures with the periodicity in the range of meters, to manipulate waves of audible frequencies, *cf.* [13] where 10^5Hz waves in phononic crystals are treated by virtue of the higher-order homogenization. The second approach based on the metamaterial design characterized by sub wavelength periodic structures is much more appropriate to attenuate acoustic waves producing undesired noise. Nonetheless, some interesting ideas of combined “hybrid resonances” in metasurfaces with the acoustic-electric energy conversion seem to be promising [14] and challenging for the optimal design of acoustic bulk metamaterials, as well as metasurfaces, [15, 16]. For that purpose, the use of the two-scale homogenization method is quite efficient as far as the scale separation between the wave lengths and the characteristic size of the microstructures holds. Two essential building block types for the design of acoustic metasurfaces include space-coiling structures and those based on the resonance effect, constituting arrays of the Helmholtz resonators. The first type elongate the travelling path of the waves through a relatively thin panel which is designed as a porous medium with large tortuosity (helical channels or labyrinth-like cascades), so that the effective behaviour is comparable with straight waveguides featured by a high refractive index, or lowered wave speed [17], *cf.* [12].

The second type, *i.e.* periodic structures incorporating the Helmholtz resonators distributed at a surface, is more suitable for devices operating at a rather narrow frequency band. It can be designed in a dual way, using the surrounding fluid itself which operates in resonance chambers – pores in the panel [18], or using compliant solid structures – mass-spring devices attached to the panel, *cf.* [19]. While for the first group the modelling is based on the poroelasticity theory, for the latter type of metamaterials and meta surfaces, the effective continuum models were proposed in [20] due to discrete lattices and the so-called Willis media with asymmetric terms in the Hooke’s law [21, 22], or approaches treating distributed resonators in the framework of the Cosserat continua, see *e.g.* [23]. As an alternative, homogenization-based modelling with the so-called high-contrast material scaling has been employed to account for anti-resonance effects in elastic media with periodically distributed soft inclusions [24, 25, 26]. Although the classical first-order homogenization method applied to the standard electrodynamics with periodically oscillating elasticity and density coefficients leads to the standard effective astronomic model describing a non dispersive medium, it has been shown that the homogenization method combined with a suitable scaling ansatz related to the contrast in the periodically oscillating elasticity coefficients leads to models of highly dispersive media due to effective anisotropic mass density depending on the frequency of imposed oscillations. Such a scaling, *i.e.* the dependence of the material coefficients on the heterogeneity size ε enables to preserve the information about the finite period of the medium when passing to the limit $\varepsilon \rightarrow 0$ [25]. In effect, the periodic heterogeneity is not smeared out in the limit completely, so that the frequency band gaps in wave propagation can be identified by negative mass density of the homogenized model [27]. The band gap sensitivity and optimization through the inclusion shape design has been considered in [28]. For plates established in the frameworks of the

Kirchhoff-Love and the Reissner-Mindlin theories, the soft inclusion metamaterial models were derived in [29]. To analyze metamaterial response to an external harmonic loading by forces with frequencies in range of the band gaps, a spectral decomposition based method has been proposed in [30].

In this paper, we build on the modelling approach reported in [9], where the vibro-acoustic transmission conditions were derived for a simple elastic plate embedded in a waveguide. Here we derive analogous conditions for “metamaterial plates” – elastic perforated plates with resonators, which are respected by periodically distributed soft inclusions. This feature completely modifies the effective model of the vibro-acoustic transmission. Equations describing a homogenized transmission layer in which the acoustic fluid-structure interaction is considered involve frequency dependent coefficients computed using characteristic responses of the representative cell which consists of the fluid and solid parts. The plate with resonators is handled using the Reissner-Mindlin kinematics according to [29]. When compared to the “standard” plate model [9], the homogenization based two scale modelling of metamaterial plate leads to complex characteristic problems parametrized by the incident wave frequency. To resolve characteristic responses of the reference cell efficiently, a spectral decomposition is employed. The vibro-acoustic transmission conditions obtained by the homogenization constitute an implicit Dirichlet-to-Neumann operator which relates the jump of the global acoustic pressure in the waveguide, as evaluated at the homogenized fictitious layer faces, with the effective acoustic momenta associated with the two faces. The proposed modelling approach provides a reduced computational model of the homogenized interface; the fluid-structure interaction problem imposed in a complex 3D geometry describing the periodic architecture of the heterogeneous plate is replaced by a 2D interface model, whereby the geometrical and mechanical features are retained. In this respect, a Bernoulli plate model obeying the Biot constitutive theory with time dependent permeability was treated recently in [31] as a “2.5” dimensional problem.

The rest of the paper is organized, as follows. In Section 2, the vibro-acoustic problem in a waveguide is introduced and a subproblem representing the transmission layer response is defined. Its homogenization is described in Section 3, whereas some technical details are explained in Appendix A and Appendix B. In Section 4, the variational formulation of the global acoustic problem is coupled with the homogenized layer through the Dirichlet-to-Neumann type conditions. Numerical implementation of the computational homogenization is reported in Section 5; some details are postponed in Appendix C. The two-scale modelling using the homogenized interface is illustrated in Section 6 where also a comparison with the “standard” plate model [9] is shown. Concluding remarks and research perspectives follow in Section 7.

Notation. In the paper, the mathematical models are formulated in a Cartesian coordinate system $\mathcal{R}(O; \mathbf{e}_1, \mathbf{e}_2, \mathbf{e}_3)$ where O is the origin of the space and $(\mathbf{e}_1, \mathbf{e}_2, \mathbf{e}_3)$ is a orthonormal basis for this space. The spatial position x in the medium is specified through the coordinates (x_1, x_2, x_3) with respect to a Cartesian reference frame \mathcal{R} . The boldface notation for vectors, $\mathbf{a} = (a_i)$, and for tensors, $\mathbf{b} = (b_{ij})$, is used. The gradient and divergence operators applied to a vector \mathbf{a} are denoted by $\nabla \mathbf{a}$ and $\nabla \cdot \mathbf{a}$, respectively. By $\nabla^S \mathbf{u}$ we denote the

symmetrized gradient $\nabla \mathbf{u}$, *i.e.* the strain tensor. When these operators have a subscript which is space variable, it is for indicating that the operator acts relatively at this space variable, for instance $\nabla_x = (\partial_i^x)$. The symbol dot ‘ \cdot ’ denotes the scalar product between two vectors and the symbol colon ‘ $:$ ’ stands for scalar (inner) product of two second-order tensors. Throughout the paper, x denotes the global (“macroscopic”) coordinates, while the “local” coordinates y describe positions within the representative unit cell $Y \subset \mathbb{R}^3$ where \mathbb{R} is the set of real numbers. By latin subscripts $i, j, k, l \in \{1, 2, 3\}$ we refer to vectorial/tensorial components in \mathbb{R}^3 , whereas subscripts $\alpha, \beta \in \{1, 2\}$ are reserved for the tangential components with respect to the plate midsurface, *i.e.* coordinates x_α of vector represented by $x' = (x_1, x_2) = (x_\alpha)$ are associated with directions $(\mathbf{e}_1, \mathbf{e}_2)$. Moreover, $\overline{\nabla}_x = (\partial_\alpha)$ is the “in-plane” gradient. The gradient in the so-called dilated configuration with coordinates (x', z) is denoted by $\hat{\nabla} = (\overline{\nabla}, \frac{1}{\varepsilon} \partial_z)$. We also use the jump w.r.t. the transversal coordinate, $\llbracket q(\cdot, x_3) \rrbracket_r^\pm = q(\cdot, r/2) - q(\cdot, -r/2)$.

2. Formulation with the large contrast elasticity plate

In this section we introduce the global problem of the acoustic wave propagation in a domain $\Omega^G \subset \mathbb{R}^3$ containing a periodically perforated plate with distributed resonators, otherwise called the metamaterial plate. We pursue the homogenization procedure proposed in [8] dealing with rigid periodically perforated plate, and further elaborated for “standard” compliant plates in [9]. The homogenized vibro-acoustic transmission conditions were derived using the asymptotic analysis w.r.t. a scale parameter ε which describes the thickness of an elastic plate when considered as a 3D object $\Sigma^\varepsilon \subset \Omega^G$, and also the characteristic size of the microstructure. For the reader’s convenience, we recall the main steps of deriving the transmission conditions for a limit global problem, as explained in detail in our previous work [9]. The global problem is formulated in a domain $\Omega^G \subset \mathbb{R}^3$ in which the perforated elastic plate of the Reissner-Mindlin type is embedded, being represented by its perforated midsurface. Then a transmission layer Ω_δ of the thickness δ is introduced via its midsurface Γ_0 , see Fig. 1 and Fig. 2. The acoustic fluid occupies domain $\Omega^{*\varepsilon} \subset \Omega_\delta$ and the associated acoustic field in Ω_δ is coupled with the one in $\Omega^G \setminus \Omega_\delta$ on the fictitious planar surfaces Γ_δ^\pm . The homogenization procedure is applied to derive an effective model of the vibro-acoustic interaction in the layer Ω_δ . In our study, the layer thickness δ is proportional to the plate heterogeneity period $\varepsilon = \delta/\varkappa$, with a given fixed $\varkappa > 0$, and also related to the plate thickness $h^\varepsilon = \varepsilon \bar{h}$ respected when describing the fluid-structure interaction on the 3D plate surface. This double role of ε is used in the asymptotic analysis the of the vibro-acoustic problem.

Finally we record the result of [9] concerning the limit global problem for the acoustic waves in the fluid interacting with the homogenized perforated plate represented by Γ_0 . In this context, a given plate thickness h is related to a given finite thickness δ_0 of the transmission layer, whereby the continuity of the acoustic fields on interfaces $\Gamma_{\delta_0}^\pm$ provides the homogenized vibro-acoustic coupling conditions prescribed on Γ_0 representing the homogenized transmission layer.

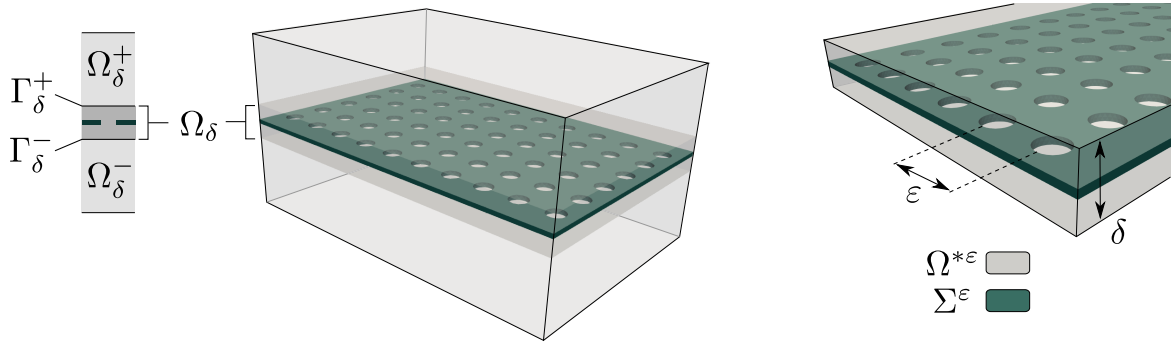


Figure 1: Transmission layer Ω_δ of thickness δ embedded in the global domain $\Omega^G = \Omega_\delta \cup \Omega_\delta^+ \cup \Omega_\delta^-$. Fluid and solid components occupy the domains $\Omega^{*\epsilon}$ and Σ^ϵ , respectively; note $\delta = \nu\epsilon$. Interface Γ_0 represent the homogenized transmission layer, see Fig. 2.

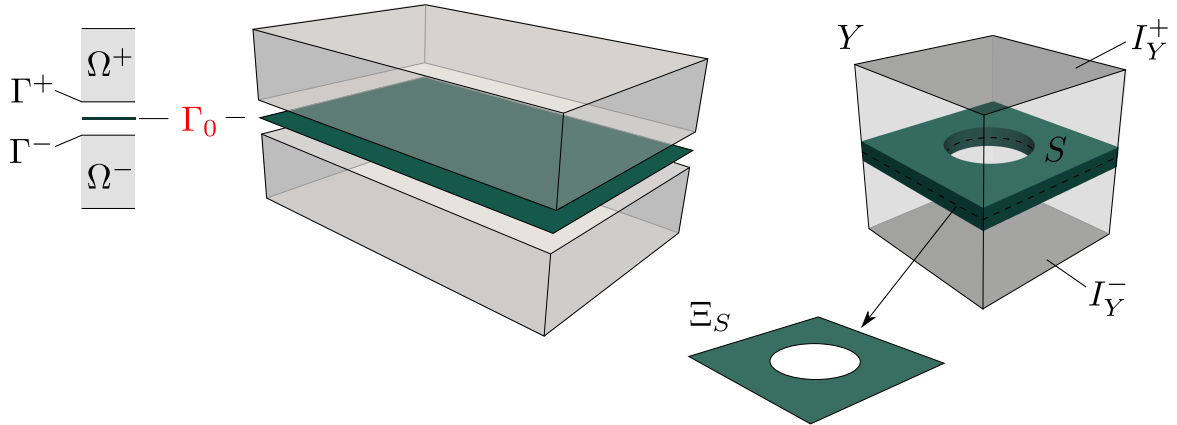


Figure 2: Left: Transmission layer Ω_δ represented by the homogenized interface Γ_0 at the macro-scale. Right: Representative 3D cell Y . The solid part S corresponds to the perforated plate – its 2D representation Ξ_S within the cell.

Knowing that parameters ε and δ may vary only proportionally as $\delta = \varkappa\varepsilon$ with a fixed $\varkappa > 0$, in what follows we drop the subscript δ when referring to geometrical objects depending on both the layer thickness and the periodic heterogeneity, thus, $\Sigma_\delta^\varepsilon \equiv \Sigma^\varepsilon$.

2.1. Geometry of the perforated layer

Let $\Gamma_0 \subset \{x \in \Omega^G | x_3 = 0\}$ be a bounded 2D planar manifold representing the plate midsurface. We define $\Omega_\delta = \Gamma_0 \times]-\delta/2, \delta/2[\subset \Omega^G$, an open bounded domain representing the transmission layer. This enables to decompose Ω^G into three nonoverlapping parts, as follows: $\Omega^G = \Omega_\delta \cup \Omega_\delta^+ \cup \Omega_\delta^-$. Thus, the transmission layer is bounded by $\partial\Omega_\delta$ which splits into three disjoint parts:

$$\partial\Omega_\delta = \Gamma_\delta^+ \cup \Gamma_\delta^- \cup \partial_{\text{ext}}\Omega_\delta, \quad \Gamma_\delta^\pm = \Gamma_0 \pm \frac{\delta}{2}\vec{e}_3, \quad \partial_{\text{ext}}\Omega_\delta = \partial\Gamma_0 \times]-\delta/2, \delta/2[, \quad (1)$$

where $\delta > 0$ is the layer thickness and $\vec{e}_3 = (0, 0, 1)$, see Fig. 3. In the context of the transmission layer definition, we consider the plate as a 3D domain Σ^ε defined in terms of the perforated midsurface Γ^ε ; the following definitions are employed:

$$\begin{aligned} \Sigma^\varepsilon &= \Gamma^\varepsilon \times \varepsilon\bar{h}] - 1/2, +1/2[, \\ \partial\Sigma^\varepsilon &= \partial_o\Sigma^\varepsilon \cup \partial_+\Sigma^\varepsilon \cup \partial_-\Sigma^\varepsilon \cup \partial_u\Sigma^\varepsilon, \end{aligned} \quad (2)$$

where

$$\begin{aligned} \partial_o\Sigma^\varepsilon &= \partial_o\Gamma^\varepsilon \times \varepsilon\bar{h}] - 1/2, +1/2[, \\ \partial_\pm\Sigma^\varepsilon &= \Gamma^\varepsilon \pm \varepsilon\bar{h}/2, \end{aligned}$$

where $\partial_u\Sigma^\varepsilon$ is the surface where the plate is clamped.

The midsurface Γ^ε representing the perforated plate is generated using a representative cell $\Xi_S \subset \mathbb{R}^2$, as a periodic lattice. Let $\Xi =]0, \ell_1[\times]0, \ell_2[$, where $\ell_1, \ell_2 > 0$ are given (usually $\ell_1 = \ell_2 = 1$) and consider the hole $\Xi^* \subset \Xi$, whereas its complement $\Xi_S = \Xi \setminus \Xi^*$ defines the solid plate segment. Then

$$\Gamma^\varepsilon = \bigcup_{k \in \mathbb{Z}^2} \varepsilon \left(\Xi_K + \sum_{i=1,2} k_i \ell_i \vec{e}_i \right) \cap \Gamma_0. \quad (3)$$

Further we introduce the representative periodic cell Y and define its solid part $S \subset Y$,

$$\begin{aligned} Y &= \Xi \times]-\varkappa/2, +\varkappa/2[, \\ S &= \Xi_S \times \bar{h}] - 1/2, +1/2[, \end{aligned} \quad (4)$$

so that $Y^* = Y \setminus \bar{S}$ is the fluid part. Obviously, in the transmission layer Ω_δ , the fluid occupies the part

$$\Omega^{*\varepsilon} = \bigcup_{k \in \mathbb{Z}^2} \varepsilon (Y^* + \sum_{i=1,2} k_i \ell_i \vec{e}_i) \cap \Omega_\delta, \quad (5)$$

where $\vec{e}_1 = (1, 0, 0)$ and $\vec{e}_2 = (0, 1, 0)$.

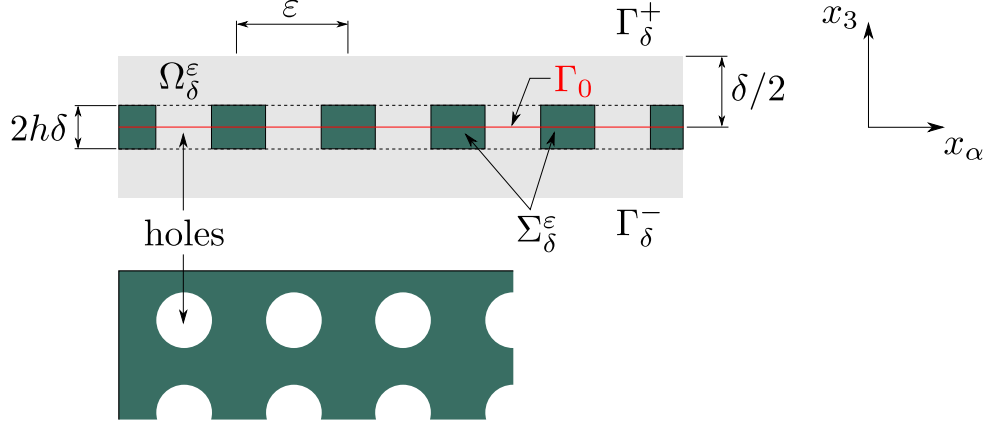


Figure 3: Scheme of the transmission layer Ω_δ in which the perforated plate $\Sigma_\delta^\varepsilon$ (dark gray) is embedded. The complementary domain $\Omega_\delta^\varepsilon$ is occupied by the acoustic fluid (light gray).

For completeness, by virtue of (2) we can introduce the decomposition of boundary $\partial S = \partial_o S \cup \partial_\pm S \cup \partial_\# S$. For this we need the boundary $\partial \Xi_S = \partial_o \Xi_S \cup \partial_\# \Xi_S$, where $\partial_\# \Xi_S \equiv \partial \Xi$, so that the closed curve $\partial_o \Xi_S = \partial \Xi^*$ generates the cylindrical boundary $\partial_o S$:

$$\begin{aligned}
\partial_o S &= \partial_o \Xi_S \times [\bar{h}] - 1/2, +1/2[, \\
\partial_\pm S &= \Xi_S \pm \vec{e}_3 \bar{h} / 2 , \\
\partial_\# S &= \partial \Xi \times [\bar{h}] - 1/2, +1/2[.
\end{aligned} \tag{6}$$

For the sake of simplicity, by $\partial \Xi_S$ we shall refer to $\partial_o \Xi_S$.

2.2. Vibro-acoustic problem in the transmission layer

The acoustic harmonic wave with the frequency ω is described by the acoustic potential $p^\varepsilon : \Omega^{*\varepsilon} \ni x \mapsto \mathbb{R}^3$ in the fluid, the corresponding wave in the elastic body is described by the displacement field $\mathbf{u}^\varepsilon : \Sigma^\varepsilon \ni x \mapsto \mathbb{R}^3$. The body is fixed to a rigid frame on the boundary $\partial_u \Sigma$ and interacting with the fluid on $\partial_* \Sigma^\varepsilon = \partial \Sigma^\varepsilon \setminus \partial_u \Sigma^\varepsilon$.

Some further notation will be employed: by c we denote the sound speed in the acoustic fluid, ρ_0 is reference fluid density, $\boldsymbol{\sigma}^\varepsilon = \mathbb{D}^\varepsilon \mathbf{e}(\mathbf{u}^\varepsilon)$ denotes the stress in the elastic solid characterized by the elasticity tensor $\mathbb{D}^\varepsilon = (D_{ijkl}^\varepsilon)$, and by $\mathbf{n} = (n_i)$ we denote the normal vector.

We shall now present the vibro-acoustic problem which will be subject of the asymptotic analysis $\varepsilon \rightarrow 0$.

Given $g^{\varepsilon\pm}$ on Γ_δ^\pm , find p^ε in $\Omega^{*\varepsilon}$ and \mathbf{u}^ε in Σ^ε , such that following equations hold: wave equations for the fluid and the solid phases:

$$\begin{aligned}
c^2 \nabla^2 p^\varepsilon + \omega^2 p^\varepsilon &= 0 & \text{in } \Omega^{*\varepsilon} , \\
\nabla \cdot \boldsymbol{\sigma}^\varepsilon(\mathbf{u}^\varepsilon) + \omega^2 \rho^\varepsilon \mathbf{u}^\varepsilon &= 0 & \text{in } \Sigma^\varepsilon ,
\end{aligned} \tag{7}$$

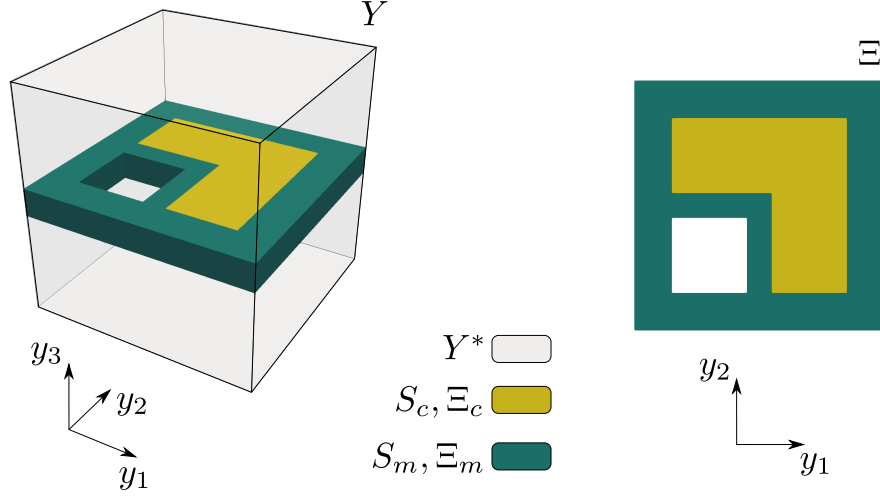


Figure 4: Representative cell Y with the solid part S and its plate representation Ξ .

fictitious interface conditions:

$$\frac{\partial p^\varepsilon}{\partial n} = -i\omega g^{\varepsilon\pm} \quad \text{on } \Gamma_\delta^\pm, \quad (8)$$

acoustic transmission:

$$\left. \begin{aligned} i\omega \mathbf{n} \cdot \mathbf{u}^\varepsilon &= \mathbf{n} \cdot \nabla p^\varepsilon \\ \mathbf{n} \cdot \boldsymbol{\sigma}^\varepsilon(\mathbf{u}^\varepsilon) &= \mathbf{b}(p^\varepsilon) = i\omega \rho_0 p^\varepsilon \mathbf{n} \end{aligned} \right\} \quad \text{on } \partial_* \Sigma^\varepsilon, \quad (9)$$

other boundary conditions for the acoustic fluid:

$$ri\omega c p^\varepsilon + c^2 \frac{\partial p^\varepsilon}{\partial n} = s2i\omega c \bar{p} \quad \text{on } \partial \Omega_\delta \setminus (\partial_u \Sigma^\varepsilon \cup \Gamma_\delta^\pm), \quad (10)$$

clamped elastic structure:

$$\mathbf{u}^\varepsilon = 0 \quad \text{on } \partial_u \Sigma^\varepsilon. \quad (11)$$

where $\partial_* \Sigma^\varepsilon = \partial \Sigma^\varepsilon \cap \partial \Omega^{*\varepsilon}$ is the surface of the elastic structure in contact with the fluid, thus, $\partial \Sigma^\varepsilon = \partial_* \Sigma^\varepsilon \cup \partial_u \Sigma^\varepsilon$. The constants $r, s \in \{0, 1\}$ and \bar{p} are defined to describe incident, reflected, or absorbed acoustic waves in the fluid, according to a selected part of the boundary.

On the interfaces Γ_δ^\pm , the acoustic fluid velocity projected into the normal $i\omega g^{\varepsilon\pm}$ is provisionally assumed to be prescribed; in fact, $g^{\varepsilon\pm}$ is an internal variable introduced when decomposing the global acoustic field into the outer one P^δ and the one defined in the layer, denoted by p^ε . In particular, one requires

$$\left. \begin{aligned} i\omega g^{\varepsilon\pm} &= \frac{\partial P^\delta}{\partial n^\pm} \quad \text{on } \Gamma_\delta^\pm, \\ p^\varepsilon &= \hat{p}^\varepsilon = P^\delta \quad \text{on } \Gamma_\delta^\pm, \end{aligned} \right\} \quad (12)$$

where n^\pm refers to normals \mathbf{n}^\pm outer to domains Ω_δ^\pm .

2.3. Plate model

Following the treatment reported in [9], instead of a 3D description of the plate, we consider the thin elastic structure being approximated by the Reissner-Mindlin plate model, thus representing the solid structure by an extended 2D continuum respecting shear stresses induced by rotations of the plate cross-sections w.r.t. the mid-plane.

The plate model can be obtained by the asymptotic analysis of the corresponding 3D elastic structure while its thickness tends to zero. However, the obtained limit plate model is then interpreted in terms of a given plate thickness h^ε , being represented by its perforated mean surface Γ^ε . Boundary $\partial_o\Gamma^\varepsilon = \partial\Gamma^\varepsilon \setminus \partial_{\text{ext}}\Gamma^\varepsilon$ describes the perforations distributed periodically with the spatial period ε . Therefore, all involved variables depend on ε . The plate deflections are described by amplitude of the membrane elastic wave $\mathbf{u}^\varepsilon = (u_1^\varepsilon, u_2^\varepsilon)$, of the transverse wave u_3^ε and of the rotation wave $\boldsymbol{\theta}^\varepsilon = (\theta_1^\varepsilon, \theta_2^\varepsilon)$. Two linear constitutive laws are involved, which depend upon the second order tensor $\mathbf{S}^\varepsilon = (S_{ij}^\varepsilon) = \varsigma\delta_{ij}$, where $\varsigma > 0$ is the shear coefficient, and the fourth order elasticity tensor $\mathbb{E}^\varepsilon = (E_{ijkl}^\varepsilon)$ which is given by the Hooke's law with tensor \mathbb{D}^ε describing the 3D elasticity model, but here adapted for the plane stress constraint. We recall that all indices $i, j, k, l = 1, 2$.

The forces $\mathbf{f} = (\bar{\mathbf{f}}, f_3)$ and $\bar{\mathbf{f}}^\partial$ applied in the plate volume and on its boundary, as well as the applied moments $\bar{\mathbf{m}}$ and $\bar{\mathbf{m}}^\partial$, depend on the acoustic potential p^ε . The crucial step in deriving the model of vibro-acoustic transmission consists in describing these forces and moments in terms of p^ε imposed on surface $\partial\Sigma^\varepsilon$ in the 3D plate representation.

The acoustic transmission layer and the plate thicknesses are employed in two contexts. Firstly, the periodically perforated plate model is defined in terms of the 2D domain $\Gamma^\varepsilon \subset \Gamma_0$ representing the mid-plane, and the thickness $h = \varepsilon_0\bar{h}$ with a fixed $\varepsilon_0 > 0$. Secondly, the interaction between the 3D elastic structure and the acoustic fluid is described in terms of the plate surface whose the thickness must be proportional to ε . Therefore, we consider $h^\varepsilon = \varepsilon\bar{h}$ and the elastic body occupying domain Σ^ε , see (2).

The homogenization of the periodically perforated plate is done by pursuing the asymptotic analysis $\varepsilon \rightarrow 0$ applied to the plate model which will be presented below. While h is fixed in the plate equation operator, being independent of ε , at the r.h.s. terms we get $1/(\varepsilon\bar{h})$ which is coherent with the dilation operation applied when dealing with fluid equation, see Section 2.7.

2.4. Forces and moments acting on the plate surface $\partial\Sigma^\varepsilon$

Due to the fluid-structure interaction, the forces and moments involved in the equations introduced below can be identified using the 3D representation of the plate surface $\partial_*\Sigma^\varepsilon$ decomposed according to (2). The actual surface traction $b_i^\varepsilon = i\omega\rho_0n_ip^\varepsilon$ is given by the acoustic potential and by the surface normal $\mathbf{n} = (n_i)$; note that $n_\alpha = 0$, $\alpha = 1, 2$ on $\partial_\pm\Sigma^\varepsilon$, whereas $n_3 = 0$ on $\partial_o\Sigma^\varepsilon$. Hence, loading the plate on its surface by the acoustic pressure yields the following expressions of forces and moments coupled with the reduced

plate degrees of freedom,

$$\begin{aligned}
\bar{f}_\alpha^\varepsilon &= 0, \quad \bar{m}_\alpha^\varepsilon = 0, \quad f_3^\partial = 0, \\
\bar{f}_3^\varepsilon &= \sum_{s=+,-} b_3(x', s\varepsilon\bar{h}/2) = i\omega\rho_0(p^\varepsilon(x', \varepsilon\bar{h}/2) - p^\varepsilon(x', -\varepsilon\bar{h}/2)), \\
f_\alpha^{\partial,\varepsilon} &= \int_{-h^\varepsilon/2}^{h^\varepsilon/2} b_\alpha(x', x_3) dx_3 = i\omega\rho_0 \int_{-h^\varepsilon/2}^{h^\varepsilon/2} n_\alpha(x') p^\varepsilon(x', x_3) dx_3, \\
m_\alpha^{\partial,\varepsilon} &= - \int_{-h^\varepsilon/2}^{h^\varepsilon/2} x_3 b_\alpha(x', x_3) dx_3 = -i\omega\rho_0 \int_{-h^\varepsilon/2}^{h^\varepsilon/2} x_3 n_\alpha(x') p^\varepsilon(x', x_3) dx_3.
\end{aligned} \tag{13}$$

Note that $\bar{f}_\alpha^\varepsilon$ and $\bar{m}_\alpha^\varepsilon$ express the volume forces which are disregarded, whereas $f_3^\partial = 0$ is the consequence of the inviscid acoustic fluid.

2.5. Fluid structure interaction on the plate surface $\partial\Sigma^\varepsilon$

The plate displacements \mathbf{w}^ε defined on the surface $\partial\Sigma^\varepsilon$ are expressed using the mid-plane kinematic fields. It holds that

$$\begin{aligned}
\mathbf{w}^\varepsilon(x', x_3) &= (w_k^\varepsilon(x', x_3)), \\
w_\alpha^\varepsilon(x', x_3) &= u_\alpha^\varepsilon(x') - x_3\theta_\alpha^\varepsilon(x'), \quad \alpha = 1, 2, \\
w_3^\varepsilon(x', x_3) &= u_3^\varepsilon(x'),
\end{aligned} \tag{14}$$

where $x' \in \Gamma^\varepsilon$, $x_3 \in \varepsilon\bar{h}] - 1/2, 1/2[$. In analogy, the test displacements $\tilde{w}_k^\varepsilon(x', x_3)$ $k = 1, 2, 3$ can be introduced in terms of the test functions $(\mathbf{v}^\varepsilon, \boldsymbol{\psi}^\varepsilon)$ involved in the weak formulation of the vibro-acoustic problem. It incorporates the virtual power

$$\int_{\partial_*\Sigma^\varepsilon} \mathbf{b}^\varepsilon \cdot \tilde{\mathbf{w}}^\varepsilon \tag{15}$$

of the external forces $\mathbf{b}^\varepsilon = i\omega\rho_0\mathbf{n}p^\varepsilon$ acting on the plate

In the equation associated with the acoustics in the fluid, the kinematic condition in $(9)_1$ prescribed on $\partial\Sigma^\varepsilon$, involves the displacement field \mathbf{w} which must be expressed in terms of the mid-plane displacements and rotations \mathbf{u}^ε and $\boldsymbol{\theta}^\varepsilon$, as introduced in (14). This yields (recall the jump $\llbracket q(\cdot, x_3) \rrbracket_{\varepsilon\bar{h}}^\pm = q(\cdot, \varepsilon\bar{h}/2) - q(\cdot, -\varepsilon\bar{h}/2)$)

$$\int_{\partial\Sigma^\varepsilon} \mathbf{n} \cdot \mathbf{w}^\varepsilon q^\varepsilon = \int_{\Gamma^\varepsilon} u_3^\varepsilon \llbracket q^\varepsilon(\cdot, x_3) \rrbracket_{\varepsilon\bar{h}}^\pm + \int_{\partial\Gamma^\varepsilon} \varepsilon\bar{h} \int_{-1/2}^{1/2} \bar{\mathbf{n}} \cdot (\mathbf{u}^\varepsilon - \varepsilon\bar{h}\zeta\boldsymbol{\theta}^\varepsilon) q^\varepsilon(\cdot, \varepsilon\bar{h}\zeta) d\zeta. \tag{16}$$

2.6. Variational formulation of the vibro-acoustic problem in the layer

In order to derive the homogenized model of the transmission layer, we shall need the variational formulation of problem (7)-(10) with the fluid-structure interaction terms (15)-(16) involving forces and moments (13).

Find $p^\varepsilon \in H^1(\Omega^{*\varepsilon})$ and $(\mathbf{u}^\varepsilon, \boldsymbol{\theta}^\varepsilon) \in (H_0^1(\Omega))^5$ such that

$$c^2 \int_{\Omega^{*\varepsilon}} \nabla p^\varepsilon \cdot \nabla q^\varepsilon - \omega^2 \int_{\Omega^{*\varepsilon}} p^\varepsilon q^\varepsilon = -i\omega c^2 \left(\int_{\Gamma^{\pm\varepsilon}} g^{\varepsilon\pm} q^\varepsilon d\Gamma + \int_{\partial\Sigma^\varepsilon} \mathbf{n} \cdot \mathbf{w}^\varepsilon q^\varepsilon d\Gamma \right), \quad (17)$$

for all $q \in H^1(\Omega^{*\varepsilon})$, where \mathbf{n} is outward normal to domain Σ^ε , and

$$\begin{aligned} & \omega^2 h \int_{\Gamma^\varepsilon} \rho \mathbf{u}^\varepsilon \cdot \mathbf{v}^\varepsilon \omega^2 \frac{h^3}{12} \int_{\Gamma^\varepsilon} \rho \boldsymbol{\theta}^\varepsilon \cdot \boldsymbol{\psi}^\varepsilon - h \int_{\Gamma^\varepsilon} [\mathbb{E}^\varepsilon \bar{\nabla}^S \mathbf{u}^\varepsilon] : \bar{\nabla}^S \mathbf{v}^\varepsilon \\ & - h \int_{\Gamma^\varepsilon} [\mathbf{S}^\varepsilon (\bar{\nabla} u_3^\varepsilon - \boldsymbol{\theta}^\varepsilon)] \cdot (\bar{\nabla} v_3^\varepsilon - \boldsymbol{\psi}^\varepsilon) - \frac{h^3}{12} \int_{\Gamma^\varepsilon} [\mathbb{E}^\varepsilon \bar{\nabla}^S \boldsymbol{\theta}^\varepsilon] : \bar{\nabla}^S \boldsymbol{\psi}^\varepsilon \\ & = \int_{\Gamma^\varepsilon} \mathbf{f}^\varepsilon(p^\varepsilon) \cdot \mathbf{v}^\varepsilon + \int_{\Gamma^\varepsilon} \bar{\mathbf{m}}^\varepsilon(p^\varepsilon) \cdot \boldsymbol{\psi}^\varepsilon + \int_{\partial_o \Gamma^\varepsilon} \bar{\mathbf{f}}^{\partial,\varepsilon}(p^\varepsilon) \cdot \bar{\mathbf{v}}^\varepsilon + \int_{\partial_o \Gamma^\varepsilon} \bar{\mathbf{m}}^{\partial,\varepsilon}(p^\varepsilon) \cdot \boldsymbol{\psi}^\varepsilon, \end{aligned} \quad (18)$$

for all test functions $(\mathbf{v}^\varepsilon, \boldsymbol{\psi}^\varepsilon) \in (H_0^1(\Omega))^5$. In (17), the displacements \mathbf{w}^ε defined on the surface $\partial\Sigma^\varepsilon$ are expressed using (16).

2.7. Dilated formulation

We can now state the vibro-acoustic problem in the dilated layer $\hat{\Omega} = \Gamma_0 \times]-\varkappa/2, +\varkappa/2[$, where the fluid occupies domain $\hat{\Omega}^* = \{(x', \varepsilon^{-1}x_3) \in \mathbb{R}^3 | x \in \Omega^{*\varepsilon}\}$, see (5). Upon introducing coordinates (x', z) in the dilated configuration, whereby $z = \varepsilon^{-1}x_3$ and $x' = (x_\alpha)$, the gradients are $\hat{\nabla} = (\partial_\alpha, \varepsilon^{-1}\partial_z)$.

Due to the transformations consisting of the dilation and the periodic unfolding, the vibro-acoustic problem can be reformulated in the domain which does not change with ε . Consequently, the standard means of convergence can be used to obtain the limit model. In the dilated configuration, we keep the same notation for all functions depending on x_3 and, thereby, on z , to simplify the notation. Thus, $\nabla p(x) = \hat{\nabla} p(x_\alpha, z)$.

Equation (17) with the substitution (16) can now be transformed by the dilatation which yields

$$\begin{aligned} & \int_{\hat{\Omega}^\varepsilon} \hat{\nabla} p^\varepsilon \cdot \hat{\nabla} q^\varepsilon - \frac{\omega^2}{c^2} \int_{\hat{\Omega}^\varepsilon} p^\varepsilon q^\varepsilon = -\frac{i\omega}{\varepsilon} \int_{\Gamma^\pm} \hat{g}^{\varepsilon\pm} q^\varepsilon \\ & - \frac{i\omega}{\varepsilon} \left[\int_{\Gamma^\varepsilon} u_3^\varepsilon \llbracket q^\varepsilon(\cdot, x_3) \rrbracket_{\varepsilon\bar{h}}^\pm + \int_{\partial_o \Gamma^\varepsilon} \varepsilon \bar{h} \int_{-1/2}^{1/2} \bar{\mathbf{n}} \cdot (\bar{\mathbf{u}}^\varepsilon - \varepsilon \bar{h} \zeta \boldsymbol{\theta}^\varepsilon) q^\varepsilon(\cdot, \varepsilon \bar{h} \zeta) d\zeta \right]. \end{aligned} \quad (19)$$

Further we employ (13) to rewrite (18) which is divided by h^ε ; the plate thickness is given for a fixed size of the heterogeneities, *i.e.* $h = \varepsilon_0 \bar{h}$. However, when dealing with the r.h.s. interaction terms, $h := h^\varepsilon = \varepsilon \bar{h}$ in accordance with the dilation transformation.

Thus, we get the plate equation in the following form

$$\begin{aligned}
& \omega^2 \int_{\Gamma^\varepsilon} \rho \mathbf{u}^\varepsilon \cdot \mathbf{v}^\varepsilon + \omega^2 \frac{h^2}{12} \int_{\Gamma^\varepsilon} \rho \boldsymbol{\theta}^\varepsilon \cdot \boldsymbol{\psi}^\varepsilon \\
& - \int_{\Gamma^\varepsilon} [\mathbb{E}^\varepsilon \bar{\nabla}^S \bar{\mathbf{u}}^\varepsilon] : \bar{\nabla}^S \bar{\mathbf{v}}^\varepsilon - \int_{\Gamma^\varepsilon} [\mathbf{S}^\varepsilon (\bar{\nabla} u_3^\varepsilon - \boldsymbol{\theta}^\varepsilon)] \cdot (\bar{\nabla} v_3^\varepsilon - \boldsymbol{\psi}^\varepsilon) - \frac{h^2}{12} \int_{\Gamma^\varepsilon} [\mathbb{E}^\varepsilon \bar{\nabla}^S \boldsymbol{\theta}^\varepsilon] : \bar{\nabla}^S \boldsymbol{\psi}^\varepsilon \\
& = \frac{i\omega\rho_0}{\varepsilon\bar{h}} \left[\int_{\Gamma^\varepsilon} v_3^\varepsilon \llbracket p^\varepsilon(\cdot, x_3) \rrbracket_{\varepsilon\bar{h}}^\pm + \varepsilon\bar{h} \int_{\partial_o\Gamma^\varepsilon} \int_{-1/2}^{1/2} p^\varepsilon(\cdot, \varepsilon\bar{h}\zeta) \bar{\mathbf{n}} \cdot (\bar{\mathbf{v}}^\varepsilon - \varepsilon\bar{h}\zeta\boldsymbol{\psi}^\varepsilon) d\zeta \right].
\end{aligned} \tag{20}$$

It is worth noting that, in (19) and (20), the r.h.s. integrals provide a symmetry of the following formulation.

The vibro-acoustic problem formulation. The acoustic response in the dilated layer $\hat{\Omega}_\delta$ is described by $(p^\varepsilon, \mathbf{u}^\varepsilon, \boldsymbol{\theta}^\varepsilon) \in H^1(\hat{\Omega}^{*\varepsilon}) \times (H_0^1(\Gamma^\varepsilon))^5$ which satisfy equations (19)-(20) for any test fields $(q^\varepsilon, \mathbf{v}^\varepsilon, \boldsymbol{\psi}^\varepsilon) \in H^1(\hat{\Omega}^{*\varepsilon}) \times (H_0^1(\Gamma^\varepsilon))^5$. The momentum fluxes depending on ε are assumed to be given in the following form

$$\begin{aligned}
\hat{g}^{\varepsilon+}(x') &= g^0(x') + \varepsilon g^{1+}(x', \frac{x'}{\varepsilon}), \\
\hat{g}^{\varepsilon-}(x') &= -g^0(x') - \varepsilon g^{1-}(x', \frac{x'}{\varepsilon}),
\end{aligned} \tag{21}$$

where $g^0 \in L^2(\Gamma_0)$ and $g^{1\pm}(x', y') \in L^2(\Gamma_0 \times \mathbb{R}^2)$, whereby $g^{1\pm}(x', \cdot)$ being Ξ -periodic in the second variable.

For any $\varepsilon > 0$ and $\hat{g}^{\varepsilon\pm}$ defined according to (21), the vibro-acoustic interaction problem constituted by equations (19)-(20) possesses a unique solution $(p^\varepsilon, \mathbf{u}^\varepsilon, \boldsymbol{\theta}^\varepsilon)$. To prove its existence and uniqueness, the *a priori* estimates must be derived in analogy with the treatment reported in [9], Appendix A, whereby the results of [29] dealing with the strongly heterogeneous Reissner-Mindlin plates must be employed, to adapt to the strong heterogeneity of the elastic properties introduced below in (24).

3. Homogenization of the transmission layer

In this section we present the two-scale limit of the vibro-acoustic problem (19)-(20). For this, in terms of the reference cell Ξ , we first introduce a strongly heterogeneous elasticity of the perforated plate. Accordingly, the asymptotic expansions are defined which enable to pass to the limit $\varepsilon \rightarrow 0$ in all integrals of the variational formulation (19)-(20) processed by the unfolding transformation, see *e.g.* [32]. We employ the unfolding operator $\mathcal{T}_\varepsilon : L^2(\Omega_\delta; \mathbb{R}) \rightarrow L^2(\Gamma_0 \times Y; \mathbb{R})$ which transforms a function $f(x)$ defined in Ω_δ into a function of two variables, $x' \in \Gamma_0$ and $y \in Y$. For any $f \in L^1(Y)$, the cell average involved in all unfolding integration formulae will be abbreviated by

$$\frac{1}{|\Xi|} \int_{\Xi} f = \underset{\Xi}{\int} f \quad \frac{1}{|\Xi|} \int_D f =: \underset{D}{\int} f, \tag{22}$$

whatever the domain $D \subset \overline{Y}$ of the the integral is (*i.e.* volume, or surface).

3.1. Heterogeneous perforated plate in the transmission layer

The plate with a periodic structure is represented by the cell $\Xi \in \mathbb{R}^2$ consisting of its solid part Ξ_S and the hole Ξ^* , see Fig. 4,

$$\begin{aligned}\Xi_S &= \Xi_m \cup \Xi_c \cup \partial\Xi_c, & \overline{\Xi_c} \cap \overline{\Xi^*} &= \emptyset, \\ S &= \Xi_S \times I_{\bar{h}}, \\ S_d &= \Xi_d \times I_{\bar{h}}, \quad d = m, c,\end{aligned}\tag{23}$$

where $I_{\bar{h}} = \bar{h}] - 1/2, +1/2[$. Note that $\partial\Xi_c \cap \partial\Xi^* = \emptyset$.

According to this split of Ξ_S the material stiffnesses and the densities of the plate are defined,

$$\begin{aligned}\mathbb{E}^\varepsilon(x) &= \chi_m^\varepsilon(x)\mathbb{E}_m + \varepsilon^2\chi_c^\varepsilon(x)\mathbb{E}_c, \\ \mathbf{S}^\varepsilon(x) &= \chi_m^\varepsilon(x)\mathbf{S}_m + \varepsilon^2\chi_c^\varepsilon(x)\mathbf{S}_c, \\ \rho^\varepsilon(x) &= \chi_m^\varepsilon(x)\rho_m + \chi_c^\varepsilon(x)\rho_c.\end{aligned}\tag{24}$$

Thus, the contrast in the elasticity is assumed, whereas the density can vary only moderately. Let us recall that this scaling ansatz has been used when analysing stop bands of the wave propagation in 3D elastic structures [25, 27] and plates [29, 30].

3.2. Limit two-scale equations of the transmission layer

Although the rigorous convergence results can be obtained, in this paper, we derive the limit model of the transmission layer using the formal asymptotic expansion method. The following truncated expansions ($p^\varepsilon, \mathbf{u}^\varepsilon, \boldsymbol{\theta}^\varepsilon$) defined in terms of unfolded fields are consistent with the convergence results supported by the a priori estimates,

$$\begin{aligned}\mathcal{T}_\varepsilon(p^\varepsilon) &= p^0(x') + \varepsilon p^1(x', y), \\ \mathcal{T}_\varepsilon(\overline{\mathbf{u}}^\varepsilon) &= \overline{\mathbf{u}}^0(x') + \varepsilon \overline{\mathbf{u}}^1(x', y') + \chi_c \hat{\mathbf{u}}(x', y'), \\ \mathcal{T}_\varepsilon(u_3^\varepsilon) &= u_3^0(x') + \varepsilon u_3^1(x', y') + \chi_c \hat{u}_3(x', y'), \\ \mathcal{T}_\varepsilon(\boldsymbol{\theta}^\varepsilon) &= \boldsymbol{\theta}^0(x') + \varepsilon \boldsymbol{\theta}^1(x', y') + \chi_c \hat{\boldsymbol{\theta}}(x', y'),\end{aligned}\tag{25}$$

where $x' \in \Gamma_0, y' \in \Xi$. In (25), all the two-scale functions are Ξ -periodic in the second variable y' , or y in the case of p ; recall that the couple $y = (y', z) \in Y$ determines positions in the reference cell Y .

We now present the limit coupled system of the plate and the acoustic fluid which governs the acoustic pressure and the plate deflections and rotations, see Appendix A for details. The response to the transverse acoustic momentum represented by g^0 and $\Delta g^1 := g^{1+} - g^{1-}$ involves the macroscopic fields $(p^0, \mathbf{u}^0, \boldsymbol{\theta}^0)$ and the two-scale functions

$(p^1, \mathbf{u}^1, \hat{\mathbf{u}}, \boldsymbol{\theta}^1, \hat{\boldsymbol{\theta}})$. For the assumed boundary conditions describing a clamped plate, the following admissibility sets are introduced,

$$\begin{aligned} \mathbb{V}^0(\Gamma_0) &= \{(\mathbf{v}, \boldsymbol{\theta}) | \bar{\mathbf{v}}, \boldsymbol{\theta} \in \mathbf{H}_0^1(\Gamma_0), v_3 \in H_0^1(\Gamma_0)\} = [H_0^1(\Gamma_0)]^5, \\ \mathbb{V}^1(\Gamma_0, \Xi_S) &= \{\mathbf{q} = (\mathbf{v}, \boldsymbol{\theta}) \in L_2(\Gamma_0) \times [H_{\#}^1(\Xi_S)]^5, \int_{\Xi_S} q_i = 0, i = 1, \dots, 5\} \quad (26) \\ \hat{\mathbb{V}}(\Gamma_0, \Xi_S) &= \{\hat{\mathbf{q}} = (\hat{\mathbf{v}}, \hat{\boldsymbol{\theta}}) \in L_2(\Gamma_0) \times [H^1(\Xi_S)]^5, \text{supp } \hat{\mathbf{q}} = \Xi_c\}. \end{aligned}$$

The plate equation holds for all test fields $(\mathbf{v}^0, \boldsymbol{\psi}^0) \in \mathbb{V}^0(\Gamma_0)$, $(\mathbf{v}^1, \boldsymbol{\psi}^1) \in \mathbb{V}^1(\Gamma_0, \Xi_S)$ and $(\hat{\mathbf{v}}, \hat{\boldsymbol{\psi}}) \in \hat{\mathbb{V}}(\Gamma_0, \Xi_S)$,

$$\begin{aligned} & -\omega^2 \int_{\Gamma_0} \int_{\Xi_S} \int_{\Xi_S} \rho_S \left((\mathbf{u}^0 + \chi_c \hat{\mathbf{u}}_3) \cdot (\mathbf{v}^0 + \chi_c \hat{\mathbf{v}}_3) + \frac{h^2}{12} (\boldsymbol{\theta}^0 + \chi_c \hat{\boldsymbol{\theta}}) \cdot (\boldsymbol{\psi}^0 + \chi_c \hat{\boldsymbol{\psi}}) \right) \\ & \int_{\Gamma_0} \left(\mathcal{P}_m((\mathbf{u}^0, \mathbf{u}^1, \boldsymbol{\theta}^0, \boldsymbol{\theta}^1), (\mathbf{v}^0, \mathbf{v}^1, \boldsymbol{\psi}^0, \boldsymbol{\psi}^1)) + \mathcal{P}_c((\hat{\mathbf{u}}, \hat{\boldsymbol{\theta}}), (\hat{\mathbf{v}}, \hat{\boldsymbol{\psi}})) \right) \\ & = \frac{i\omega\rho_0}{\hbar} \int_{\Gamma_0} \left(v_3^0 \int_{\Xi_S} \llbracket p^1 \rrbracket_{\hbar}^{\pm} + \int_{\Xi_c} \hat{v}_3 \llbracket p^1 \rrbracket_{\hbar}^{\pm} \right) \\ & + i\omega\rho_0 \int_{\Gamma_0} \left(\bar{\mathbf{v}}^0 \cdot \int_{-1/2}^{1/2} \int_{\partial\Xi_S} \bar{\mathbf{n}} p^1 + p^0 \int_{\partial\Xi_S} \bar{\mathbf{v}}^1 \cdot \bar{\mathbf{n}} \right), \end{aligned} \quad (27)$$

where, at the l.h.s. , the abstract notation \mathcal{P}_m and \mathcal{P}_c introduced in (A.5) represent operators associated with the plate elasticity. The fluid is governed by the following equation to hold for all $q^0 \in H^1(\Gamma_0)$ and $q^1 \in H_{\#}^1(Y^*)$,

$$\begin{aligned} & c^2 \int_{\Gamma_0} \int_{Y^*} (\bar{\nabla}_x p^0 + \bar{\nabla}_y p^1) \cdot (\bar{\nabla}_x q^0 + \bar{\nabla}_y q^1) + c^2 \int_{\Gamma_0} \int_{Y^*} \partial_z p^1 \partial_z q^1 - \omega^2 \int_{\Gamma_0} \int_{Y^*} p^0 q^0 \\ & = -i\omega c^2 \int_{\Gamma_0} \left[q^0 \int_{\Xi} \Delta g^1 + g^0 \left(\int_{I_y^+} q^1 - \int_{I_y^-} q^1 \right) \right. \\ & \left. + u_3^0 \int_{\Xi_S} \llbracket q^1 \rrbracket_{\hbar}^{\pm} + \bar{\mathbf{u}}^0 \cdot \int_{\partial\Xi_S} \bar{\mathbf{n}} \bar{h} \int_{-1/2}^{1/2} q^1 d\zeta + q^0 \bar{h} \int_{\partial\Xi_S} \bar{\mathbf{n}} \cdot \bar{\mathbf{u}}^1 + \int_{\Xi_c} \hat{u}_3 \llbracket q^1 \rrbracket_{\hbar}^{\pm} \right], \end{aligned} \quad (28)$$

recalling the abbreviation $\Delta g^1 = g^{1+} - g^{1-}$.

3.3. Local problems

We consider a fix position $x' \in \Gamma_0$. The local problems are identified in the limit equations (27)-(28) for vanishing macroscopic test fields, *i.e.* upon substituting there $\mathbf{v}^0 \equiv \mathbf{0}$, $\boldsymbol{\psi}^0 \equiv \mathbf{0}$ and $q^0 \equiv 0$. In doing so, the system is decomposed into two subsystems which can be solved independently for a given macroscopic responses. Furthermore, due to the linearity of the obtained equations for unknowns comprising macroscopic fields and two-scale fields, the latter fields can be decomposed using a multiplicative split into the macroscopic variables and the characteristic responses.

3.3.1. Characteristic responses of the fluid and soft inclusions in the plate

These characteristic responses describe dynamic properties of the two-phase heterogeneous structure where the soft inclusions constitute a kind of resonators. The first group of autonomous local problems imposed in $Y^* \times \Xi_c$ for $(p^1(x', \cdot), u_3(x', \cdot)) \in W_{\#}$, where $W_{\#} = H_0^1(\Xi_c) \times H_{\#}^1(Y^*)$, is extracted from (27)-(28) while vanishing macroscopic test functions and all two-scale test function except of q^1 and \hat{v}_3 ,

$$\begin{aligned} & \int_{Y^*} \hat{\nabla}_y p^1 \cdot \hat{\nabla}_y q^1 + i\omega \int_{\Xi_c} \hat{u}_3 \llbracket q^1 \rrbracket_{\bar{h}}^{\pm} = - \int_{Y^*} \hat{\nabla}_y q^1 \cdot \hat{\nabla}_y y_{\alpha} \partial_{\alpha}^x p^0 \\ & - i\omega \left[g^0 \left(\int_{I_y^+} q^1 - \int_{I_y^-} q^1 \right) + u_3^0 \int_{\Xi_S} \llbracket q^1 \rrbracket_{\bar{h}}^{\pm} + \bar{\mathbf{u}}^0 \cdot \int_{\partial \Xi_S} \bar{\mathbf{n}} \bar{h} \int_{-1/2}^{1/2} q^1 d\zeta \right], \quad (29) \\ & \int_{\Xi_c} ([\mathbf{S}_c \bar{\nabla}_y \hat{u}_3] \cdot \bar{\nabla}_y \hat{v}_3 - \omega^2 \rho_c \hat{u}_3 \hat{v}_3) - \frac{i\omega \rho_0}{\bar{h}} \int_{\Xi_c} \hat{v}_3 \llbracket p^1 \rrbracket_{\bar{h}}^{\pm} = \omega^2 u_3^0 \int_{\Xi_c} \rho_c \hat{v}_3, \end{aligned}$$

for all $(q^1, \hat{v}_3) \in W_{\#}$. By virtue of the linearity of (29), (p^1, \hat{u}_3) can be expressed using the linear combinations of the macroscopic variables $(\partial_{\beta}^x p^0, g^0, \mathbf{u}^0)$ and the characteristic response functions π^{β}, ξ and η^k , $\beta = 1, 2, k = 1, 2, 3$,

$$\begin{aligned} p^1(x', y) &= \pi^{\beta}(y) \partial_{\beta}^x p^0(x') + i\omega \xi(y) g^0(x') + i\omega \eta^k(y) u_k^0(x'), \\ \hat{u}_3(x', y) &= \hat{w}^{\beta}(y) \partial_{\beta}^x p^0(x') + i\omega \hat{\zeta}(y) g^0(x') + i\omega \hat{\varpi}^k(y) u_k^0(x'). \end{aligned} \quad (30)$$

Using the following inner products and bilinear forms,

$$\begin{aligned} \hat{b}_c(\hat{w}, \hat{z}) &= \int_{\Xi_c} [\mathbf{S}_c \nabla_y \hat{w}] \cdot \nabla_y \hat{z}, \\ \int_{\Xi_c} \mathbf{u} \cdot \mathbf{v} &= \int_{\Xi_c} \mathbf{u} \cdot \mathbf{v}, \\ \int_{Y^*} \mathbf{u} \cdot \mathbf{v} &= \int_{Y^*} \mathbf{u} \cdot \mathbf{v}, \end{aligned} \quad (31)$$

we define operator $\mathcal{T}_{i\omega}$, which is employed in the problems for the characteristic responses,

$$\begin{aligned} \langle \langle \mathcal{T}_{i\omega}(\hat{w}, \hat{p}), (\hat{v}, \hat{q}) \rangle \rangle_c &= \frac{\bar{h}}{\rho_0} \left[\hat{b}_c(\hat{w}, \hat{v}) - \omega^2 \int_{\Xi_c} \rho \hat{w} \cdot \hat{v} \right] \\ & - i\omega \int_{\Xi_c} \hat{v} \cdot \llbracket \hat{p} \rrbracket_{\bar{h}}^{\pm} + i\omega \int_{\Xi_c} \hat{w} \cdot \llbracket \hat{q} \rrbracket_{\bar{h}}^{\pm} + \int_{Y^*} \nabla_y \hat{p} \cdot \nabla_y \hat{q}. \end{aligned} \quad (32)$$

We can now introduce the local problems related to the fluid and fluid-solid interaction which enable to compute the characteristic responses involved in (30).

1. Find $(\hat{w}^{\beta}, \pi^{\beta}) \in W_{\#}$, such that

$$\langle \langle \mathcal{T}_{i\omega}(\hat{w}^{\beta}, \pi^{\beta}), (\hat{v}, q) \rangle \rangle_c = - \int_{Y^*} \bar{\nabla}_y y_{\beta} \cdot \bar{\nabla}_y q, \quad \forall (\hat{v}, q) \in W_{\#}. \quad (33)$$

2. Find $(\hat{\zeta}, \xi) \in W_{\#}$, such that

$$\langle \langle \mathcal{T}_{i\omega}(\hat{\zeta}, \xi), (\hat{v}, q) \rangle \rangle_c = - \left(\int_{I_y^+} q - \int_{I_y^-} q \right), \quad \forall (\hat{v}, q) \in W_{\#}. \quad (34)$$

3. Find $(\hat{\omega}^\alpha, \eta^\alpha) \in W_{\#}$, such that

$$\langle \langle \mathcal{T}_{i\omega}(\hat{\omega}^\alpha, \eta^\alpha), (\hat{v}, q) \rangle \rangle_c = -\bar{h} \int_{\partial\Xi_S} n_\alpha \int_{-1/2}^{1/2} q(\cdot, \zeta) d\zeta, \quad \forall (\hat{v}, q) \in W_{\#}. \quad (35)$$

4. Find $(\hat{\omega}^3, \eta^3) \in W_{\#}$, such that

$$\langle \langle \mathcal{T}_{i\omega}(\hat{\omega}^3, \eta^3), (\hat{v}, q) \rangle \rangle_c = -i\omega \frac{\bar{h}}{\rho_0} \int_{\Xi_c} \rho \hat{v} - \int_{\Xi_S} \llbracket q \rrbracket_h^\pm \cdot 1, \quad \forall (\hat{v}, q) \in W_{\#}. \quad (36)$$

For the particular type of structures considered in this study, some of the above problems can be simplified due to the vanishing part of the solution.

Definition 1. Cell Y decomposed in the fluid part Y^* and the solid part S is called z -symmetric, if

$$(y', z) \in Y^* \Leftrightarrow (y', -z) \in Y^*, \text{ and } (y', z) \in \partial Y^* \Leftrightarrow (y', -z) \in \partial Y^*. \quad (37)$$

□

Although the z -symmetry property is related directly to the cell decomposition rather than to the cell Y itself, the notion of z -symmetry applies in the context of Y and its decomposition.

Definition 2. Let Y is z -symmetric. Function q defined in $Y_d \subset Y$, with traces defined on ∂Y_d is called z -symmetric, if

$$q(y', z) = q(y', -z) \text{ for any } (y', z) \in \bar{Y}_d. \quad (38)$$

□

Lemma 1. For any z -symmetric function q , $\llbracket q \rrbracket_h^\pm = 0$ so that $\int_{\Xi_S} v \cdot \llbracket q \rrbracket_h^\pm = 0$ for any $v \in H^1(\Xi_c)$. As the result, the characteristic deflections in problems (33) and (35) vanish.

Proposition 1. Let Y be z -symmetric. Then problems (33) and (35) can be reformulated in terms of the characteristic pressures π^β and η^α only, which satisfy

$$\int_{Y^*} \nabla_y(\pi^\alpha + y_\alpha) \cdot \nabla_y \hat{q} = 0 \quad \forall q \in H_{\#}^1(Y^*), \quad (39)$$

$$\int_{Y^*} \nabla_y \eta^\alpha \cdot \nabla_y \hat{q} = -\bar{h} \int_{\partial\Xi_S} n_\alpha \int_{-1/2}^{1/2} q(\cdot, \zeta) d\zeta \quad \forall q \in H_{\#}^1(Y^*), \quad (40)$$

whereby $\hat{w}^\beta = \hat{\omega}^\alpha \equiv 0$.

The proof is based on Lemma 1. It can be seen, that solutions π^α and η^α are z -symmetric, so that equations in (33) and (35) are satisfied with vanishing \hat{w}^β and $\hat{\omega}^\alpha$.

In this paper, we consider a z -symmetric cell Y , so that Proposition 1 applies. However, for the sake of generality, we shall keep the formulations (33) and (35). This will induce a general set of homogenized effective tensors involved in the macromodel. Due to the z -symmetry, some components of these coefficients vanish. In future studies, we intend to consider plates with more complex perforations, such that the z -symmetry will not apply.

The second group of autonomous local problems is imposed in the soft plate inclusions Ξ_c and governs in-plane displacements $\hat{\mathbf{u}}$ and rotations $\hat{\boldsymbol{\theta}}$, whereby the only nonvanishing test functions are $\hat{\mathbf{v}}$ and $\hat{\boldsymbol{\psi}}$. The following identities related to the dynamic properties are to be satisfied by $\hat{\boldsymbol{\theta}}(x, \cdot) \in \mathbf{H}_0^1(\Xi_c)$, $\hat{u}_\alpha \in H_0^1(\Xi_c)$,

$$\begin{aligned} a_c(\hat{\boldsymbol{\theta}}, \hat{\boldsymbol{\psi}}) - \omega^2 \int_{\Xi_c} \rho(\hat{\boldsymbol{\theta}} + \boldsymbol{\theta}^0) \cdot \hat{\boldsymbol{\psi}} &= 0, \quad \forall \hat{\boldsymbol{\psi}} \in \mathbf{H}_0^1(\Xi_c), \\ a_c(\hat{\mathbf{u}}, \hat{\boldsymbol{\psi}}) - \omega^2 \int_{\Xi_c} \rho(\hat{\mathbf{u}} + \bar{\mathbf{u}}^0) \cdot \hat{\boldsymbol{\psi}} &= 0, \quad \forall \hat{\boldsymbol{\psi}} \in \mathbf{H}_0^1(\Xi_c), \end{aligned} \quad (41)$$

where

$$a_c(\bar{\mathbf{u}}, \bar{\mathbf{v}}) = \int_{\Xi_c} [\mathbb{E}_c \mathbf{e}_y(\bar{\mathbf{u}})] : \mathbf{e}_y(\bar{\mathbf{v}}). \quad (42)$$

Both problems in (41) yield the following eigenvalue problem: Find $(\boldsymbol{\Theta}^r, \lambda^r) \in \mathbf{H}_0^1 \times \mathbb{R}$ for $r = 1, 2, \dots$, such that

$$a_c(\boldsymbol{\Theta}^r, \hat{\boldsymbol{\psi}}) = \lambda^r \int_{\Xi_c} \rho \boldsymbol{\Theta}^r \cdot \hat{\boldsymbol{\psi}}, \quad \forall \hat{\boldsymbol{\psi}} \in \mathbf{H}_0^1(\Xi_c), \quad (43)$$

so that the local responses are expressed in the bases constituted by the eigenfunctions

$$\hat{\boldsymbol{\theta}} = \sum_{r \geq 1} c^r \boldsymbol{\Theta}^r, \quad \hat{\mathbf{u}} = \sum_{r \geq 1} \bar{c}^r \boldsymbol{\Theta}^r, \quad (44)$$

where the coefficients c^r and \bar{c}^r are given by

$$c^k = \frac{\omega^2}{\lambda^k - \omega^2} \int_{\Xi_c} \rho \boldsymbol{\Theta}^k \cdot \boldsymbol{\theta}^0, \quad \bar{c}^k = \frac{\omega^2}{\lambda^k - \omega^2} \int_{\Xi_c} \rho \boldsymbol{\Theta}^k \cdot \bar{\mathbf{u}}^0. \quad (45)$$

3.3.2. Characteristic responses associated with the plate stiffness

Local problems characterizing the static elasticity of the plate associated with the normal and shear strains arise from (27) for nonvanishing test functions \mathbf{v}^1 and $\boldsymbol{\psi}^1$. These problems can be expressed using the bilinear forms

$$\begin{aligned} a_m(\bar{\mathbf{u}}, \bar{\mathbf{v}}) &= \int_{\Xi_m} [\mathbb{E}_m \bar{\nabla}_y^S \bar{\mathbf{u}}] : \bar{\nabla}_y^S \bar{\mathbf{v}}, \\ b_m(w, z) &= \int_{\Xi_m} [\mathbf{S}_m \nabla_y w] \cdot \nabla_y z, \end{aligned} \quad (46)$$

and in terms of coordinate combinations $\mathbf{\Pi}^{\alpha\beta} = (\Pi_\nu^{\alpha\beta})$, $\Pi_\nu^{\alpha\beta} = y_\beta \delta_{\alpha\nu}$ with $\nu, \alpha, \beta = 1, 2$, so that $\bar{\nabla}_x^S \bar{\mathbf{u}}^0 = \bar{\nabla}_y^S \mathbf{\Pi}^{\alpha\beta} \partial_\alpha^x \bar{u}_\beta^0$. For a fixed $x' \in \Gamma_0$, functions $\boldsymbol{\theta}^1(x', \cdot), \bar{\mathbf{u}}^1(x', \cdot) \in [H_\#^1(\Xi_m)]^2$ and $u_3^1(x', \cdot) \in H_\#^1(\Xi_m)$ satisfy

$$\begin{aligned} a_m(\boldsymbol{\theta}^1 + \mathbf{\Pi}^{\alpha\beta} \partial_\alpha^x \theta_\beta^0, \boldsymbol{\psi}^1) &= 0, \quad \forall \boldsymbol{\psi}^1 \in [H_\#^1(\Xi_m)]^2, \\ a_m(\bar{\mathbf{u}}^1 + \mathbf{\Pi}^{\alpha\beta} \partial_\alpha^x \bar{u}_\beta^0, \bar{\mathbf{v}}^1) &= i\omega\rho_0 \int_{\Gamma_0} p^0 \int_{\partial\Xi_S} \bar{\mathbf{n}} \cdot \bar{\mathbf{v}}^1, \quad \forall \bar{\mathbf{v}}^1 \in [H_\#^1(\Xi_m)]^2, \\ b_m(u_3^1 + y_\alpha (\partial_\alpha^x u_3^0 - \theta_\alpha^0), v_3^1) &= 0, \quad \forall v_3^1 \in H_\#^1(\Xi_m); \end{aligned} \quad (47)$$

Again using the linearity of (47), for the two-scale depending on the macroscopic responses $\bar{\nabla}_x^S \bar{\mathbf{u}}^0, \bar{\nabla}_x^S \boldsymbol{\theta}^0, \bar{\nabla}_x u_3$, and p^0 , the following multiplicative decompositions can be introduced

$$\bar{\mathbf{u}}^1 = \bar{\chi}^{\alpha\beta} (\bar{\nabla}_x^S \bar{\mathbf{u}}^0)_{\alpha\beta} + \bar{\chi}^* i\omega\rho_0 p^0, \quad (48)$$

$$u_3^1 = \chi^k ((\bar{\nabla}_x u_3)_k - \theta_k), \quad (49)$$

$$\boldsymbol{\theta}^1 = \bar{\chi}^{\alpha\beta} (\bar{\nabla}_x^S \boldsymbol{\theta}^0)_{\alpha\beta}, \quad (50)$$

involving the local characteristic responses $\bar{\chi}^{\alpha\beta}, \bar{\chi}^* \in \mathbf{H}_\#^1(\Xi_m)$, and $\chi^k \in H_\#^1(\Xi_m)$, usually called the corrector functions. It is worth noting that the same functions $\bar{\chi}^{\alpha\beta}$ are involved in both $\bar{\mathbf{u}}^1$ and $\boldsymbol{\theta}^1$ due to the similar structure of (47)₁ and (47)₂. The following three local autonomous problems have to be solved,

- Find $\bar{\chi}^{\alpha\beta} \in \mathbf{H}_\#^1(\Xi_m)/\mathbb{R}^2$ such that

$$a_m(\bar{\chi}^{\alpha\beta} + \mathbf{\Pi}^{\alpha\beta}, \bar{\mathbf{v}}) = 0 \quad \forall \bar{\mathbf{v}} \in \mathbf{H}_\#^1(\Xi_m). \quad (51)$$

- Find $\chi^\alpha \in H_\#^1(\Xi_m)/\mathbb{R}$ such that

$$b_m(\chi^\alpha + y_\alpha, \tilde{z}) = 0 \quad \forall \tilde{z} \in H_\#^1(\Xi_m), \quad \alpha = 1, 2. \quad (52)$$

- Find $\bar{\chi}^* \in \mathbf{H}_\#^1(\Xi_m)/\mathbb{R}^2$ such that

$$a_m(\bar{\chi}^*, \bar{\mathbf{v}}) = \int_{\partial\Xi_S} \bar{\mathbf{n}} \cdot \bar{\mathbf{v}}, \quad \forall \bar{\mathbf{v}} \in \mathbf{H}_\#^1(\Xi_m). \quad (53)$$

3.4. Macroscopic model equations

In the limit equations (27)-(28), we now consider nonvanishing the macroscopic test functions $\mathbf{v}^0, \boldsymbol{\psi}^0$ and q^0 only, whereas all other test functions vanish. Thus, the following equations which describe behaviour of the plate and the fluid in the fictitious layer, are

obtained, such that

$$\begin{aligned}
& -\omega^2 \int_{\Gamma_0} \int_{\Xi_S} \rho_S \left((\mathbf{u}^0 + \chi_c \hat{\mathbf{u}}) \cdot \mathbf{v}^0 + \frac{h^2}{12} (\boldsymbol{\theta}^0 + \chi_c \hat{\boldsymbol{\theta}}) \cdot \boldsymbol{\psi}^0 \right) \\
& + \int_{\Gamma_0} \left(\int_{\Xi_m} [\mathbb{E}_m(\bar{\nabla}_x^S \bar{\mathbf{u}}^0 + \bar{\nabla}_y^S \bar{\mathbf{u}}^1)] : \bar{\nabla}_x^S \bar{\mathbf{v}}^0 + \int_{\Xi_m} [\mathbf{S}_m(\bar{\nabla}_x u_3^0 + \bar{\nabla}_y u_3^1 - \boldsymbol{\theta}^0)] \cdot \boldsymbol{\psi}^0 \right) \\
& + \frac{h^2}{12} \int_{\Gamma_0} \left(\int_{\Xi_m} [\mathbb{E}_m(\bar{\nabla}_x^S \boldsymbol{\theta}^0 + \bar{\nabla}_y^S \boldsymbol{\theta}^1)] : \bar{\nabla}_x^S \boldsymbol{\psi}^0 \right) \\
& = \frac{i\omega\rho_0}{\bar{h}} \int_{\Gamma_0} v_3^0 \int_{\Xi_S} \llbracket p^1 \rrbracket_{\bar{h}}^\pm + i\omega\rho_0 \int_{\Gamma_0} \bar{\mathbf{v}}^0 \cdot \int_{-1/2}^{1/2} \int_{\partial\Xi_S} \bar{\mathbf{n}} p^1,
\end{aligned} \tag{54}$$

holds for all couples $(\mathbf{v}^0, \boldsymbol{\psi}^0) \in \mathbb{V}^0$, and

$$\begin{aligned}
& c^2 \int_{\Gamma_0} \int_{Y^*} (\bar{\nabla}_x p^0 + \bar{\nabla}_y p^1) \cdot \bar{\nabla}_x q^0 - \omega^2 \int_{\Gamma_0} \int_{Y^*} p^0 q^0 \\
& = -i\omega c^2 \int_{\Gamma_0} q_0 \left(\int_{\Xi} \Delta g^1 + \bar{h} \int_{\partial\Xi_S} \bar{\mathbf{n}} \cdot \bar{\mathbf{u}}^1 \right),
\end{aligned} \tag{55}$$

holds for all $q^0 \in L^2(\Gamma_0)$.

3.4.1. Homogenized coefficients

We shall first identify homogenized coefficients in the fluid equation (55). Upon substituting there the multiplicative splits (30) and (48), it yields

$$\begin{aligned}
A_{\alpha\beta} &= \int_{Y^*} \nabla_y(\pi^\beta + y_\beta) \cdot \nabla_y y_\alpha = \int_{Y^*} \nabla_y(\pi^\beta + y_\beta) \cdot \nabla_y(\pi^\alpha + y_\alpha), \\
B_\alpha &= \int_{Y^*} \partial_\alpha^y \xi, \\
D_{\alpha k}^* &= \int_{Y^*} \partial_\alpha^y \eta^k, \\
H_{\alpha\beta} &= \int_{\partial\Xi_S} \bar{\mathbf{n}} \cdot \bar{\boldsymbol{\chi}}^{\alpha\beta}, \\
K &= \int_{\partial\Xi_S} \bar{\mathbf{n}} \cdot \bar{\boldsymbol{\chi}}^*.
\end{aligned} \tag{56}$$

The homogenized coefficients $\mathbf{A} = (A_{\alpha\beta})$, $\mathbf{B} = (B_\alpha)$, and $\mathbf{D}^* = (D_k^*)$, are associated with the integral involving p^1 , whereas $\mathbf{H} = (H_{\alpha\beta})$ and K are identified in the last r.h.s. integral involving $\bar{\mathbf{u}}^1$.

Now the homogenized fluid equation (55) can be rewritten in terms of the coefficients

(56). It is satisfied by macroscopic functions $(p^0, g^0, \mathbf{u}^0) \in H^1(\Gamma_0) \times L^2(\Gamma_0) \times \mathbf{H}^1(\Gamma_0)$,

$$\begin{aligned} & c^2 \int_{\Gamma_0} (\mathbf{A} \bar{\nabla}_x p^0) \cdot \bar{\nabla}_x q^0 - \zeta^* \omega^2 \int_{\Gamma_0} p^0 q^0 + i\omega c^2 \int_{\Gamma_0} g^0 \mathbf{B} \cdot \bar{\nabla}_x q^0 + i\omega c^2 \int_{\Gamma_0} \bar{\nabla}_x q^0 \cdot \mathbf{D}^* \mathbf{u}^0 \\ &= -i\omega c^2 \bar{h} \int_{\Gamma_0} q^0 \left(\frac{\Delta G^1}{\bar{h}} + i\omega \rho_0 K p^0 + \mathbf{H} : \bar{\nabla}_x^S \mathbf{u}^0 \right), \end{aligned} \quad (57)$$

for all $q^0 \in H^1(\Gamma_0)$, where $\zeta^* = |Y^*|/|\Xi|$ and $\Delta G^1 = |\Xi|^{-1} \int_{\Xi} \Delta g^1$. Recall that the transversal momentum flux difference Δg^1 was introduced in (28). In Section 4, we shall establish g^0 and Δg^1 using averaged momentum fluxes \hat{G}_0^\pm associated with the interfaces Γ^\pm , see Fig. 2.

Further we consider the plate equation (54) and denote $\gamma := \frac{\bar{h}}{\rho_0}$ which will be involved in some of the following expressions for the homogenized coefficients. The inertia terms associated with the plate in-plane velocities and cross-sectional rotations can be expressed using the homogenized mass coefficients $\tilde{\mathcal{M}} = (\mathcal{M}_{\alpha\beta})$,

$$\begin{aligned} & \int_{\Xi_S} \rho_S (\bar{\mathbf{u}}^0 + \chi_c \hat{\mathbf{u}}) \cdot \bar{\mathbf{v}}^0 = v_\alpha^0 \tilde{\mathcal{M}}_{\alpha\beta} u_\beta^0, \\ & \int_{\Xi_S} \rho_S (\boldsymbol{\theta}^0 + \chi_c \hat{\boldsymbol{\theta}}) \cdot \boldsymbol{\psi}^0 = \psi_\alpha^0 \tilde{\mathcal{M}}_{\alpha\beta} \theta_\beta^0, \end{aligned} \quad (58)$$

where $\tilde{\mathcal{M}}$ is identified upon substituting (44)-(45) in (58),

$$\gamma^{-1} \tilde{\mathcal{M}}_{\alpha\beta} = \int_{\Xi_S} \rho_S \delta_{\alpha\beta} - \sum_{r \geq 1} \frac{\omega^2}{\omega^2 - \lambda^r} \int_{\Xi_c} \rho \Theta_\alpha^r \int_{\Xi_c} \rho \Theta_\beta^r. \quad (59)$$

To proceed, in (54), we consider the integrals related to the elasticity, as represented by tensors \mathbb{E}_m and \mathbf{S}_m , which can be expressed using the effective elasticity tensors $\mathbb{E}^H = (E_{\alpha\beta\mu\nu}^H)$ and $\mathbf{S}^H = (S_{\alpha\beta}^H)$, and using the pressure-strain coupling tensor $\mathbf{H}^* = (H_{\alpha\beta})$ defined, as follows

$$\begin{aligned} E_{\alpha\beta\mu\nu}^H &= \int_{\Xi_m} \mathbb{E}_m \bar{\nabla}_y^S (\bar{\chi}^{\mu\nu} + \mathbf{\Pi}^{\mu\nu}) : \bar{\nabla}_y^S (\bar{\chi}^{\alpha\beta} + \mathbf{\Pi}^{\alpha\beta}), \\ S_{\alpha\beta}^H &= \int_{\Xi_m} [\mathbf{S}_m \nabla_y (\chi^\alpha + y_\alpha)] \cdot \nabla_y (\chi^\beta + y_\beta), \\ H_{\alpha\beta}^* &= - \int_{\Xi_m} \mathbb{E}_m \bar{\nabla}_y^S \bar{\chi}^* : \bar{\nabla}_y^S \bar{\chi}^{\alpha\beta}. \end{aligned} \quad (60)$$

The above expressions can be obtained using the split forms (48)-(50).

Now we shall consider the other terms in (54). These are related to the transverse inertia due to the plate deflections, and to the r.h.s. terms describing the fluid-structure

interaction. The following expressions are obtained upon substituting there the split form of two-scale functions, see (30) and (48)-(50),

$$\begin{aligned}
& -\omega^2 \int_{\Xi_S} \rho_S (\hat{u}_3^0 + \chi_c [\hat{w}^\beta \partial_\beta p^0 + i\omega \hat{\zeta} g^0 + i\omega \hat{\omega}^k u_k^0]) v_3^0 \\
& - \frac{i\omega \rho_0}{\hbar} v_3^0 \int_{\Xi_S} [\pi^\beta \partial_\beta^x p^0 + i\omega \xi g^0 + i\omega \eta^k u_k^0]_{\hbar}^{\pm} \\
& - i\omega \rho_0 v_\alpha^0 \int_{\partial \Xi_S} n_\alpha \int_{-1/2}^{1/2} (\pi^\beta \partial_\beta^x p^0 + i\omega \xi g^0 + i\omega \eta^k u_k^0) \\
& = \omega^2 v_3^0 u_3^0 \underbrace{\left[\frac{\rho_0}{\hbar} \int_{\Xi_S} [\eta^3]_{\hbar}^{\pm} - \int_{\Xi_S} \rho_S (1 + i\omega \chi_c \hat{\omega}^3) \right]}_{-\gamma^{-1} M_{33}} \\
& + \omega^2 v_3^0 u_\alpha^0 \underbrace{\left[\frac{\rho_0}{\hbar} \int_{\Xi_S} [\eta^\alpha]_{\hbar}^{\pm} - i\omega \int_{\Xi_c} \rho_c \hat{\omega}^\alpha \right]}_{-\gamma^{-1} M_{3\alpha}} \\
& + \omega^2 v_\alpha^0 u_k^0 \underbrace{\left[\rho^0 \int_{\partial \Xi_S} n_\alpha \int_{-1/2}^{1/2} \eta^k \right]}_{-\gamma^{-1} M_{\alpha k}} \tag{61} \\
& - i\omega v_3^0 \partial_\beta p^0 \underbrace{\frac{\rho_0}{\hbar} \left[\int_{\Xi_S} [\pi^\beta]_{\hbar}^{\pm} - i\omega \frac{\bar{h}}{\rho_0} \int_{\Xi_c} \rho_c \hat{w}^\beta \right]}_{\gamma^{-1} D_{3\beta}} \\
& - i\omega v_\alpha^0 \partial_\beta p^0 \underbrace{\frac{\rho_0}{\hbar} \left[\bar{h} \int_{\partial \Xi_S} n_\alpha \int_{-1/2}^{1/2} \pi^\beta \right]}_{\gamma^{-1} D_{\alpha\beta}} \\
& + \omega^2 v_3^0 g^0 \underbrace{\frac{\rho_0}{\hbar} \left[\int_{\Xi_S} [\xi]_{\hbar}^{\pm} - i\omega \frac{\bar{h}}{\rho_0} \int_{\Xi_c} \rho_c \hat{\zeta} \right]}_{\gamma^{-1} C_3} + \omega^2 v_\alpha^0 g^0 \underbrace{\rho_0 \int_{\partial \Xi_S} n_\alpha \int_{-1/2}^{1/2} \xi}_{\gamma^{-1} C_\alpha}
\end{aligned}$$

Note that $\rho_0 = \gamma^{-1} \bar{h}$, which can be employed in the definition of C_α and $M_{\alpha k}$.

It is now possible to define the homogenized mass tensor,

$$\mathbf{L} = \begin{bmatrix} (\tilde{\mathcal{M}}_{\alpha\beta} + M_{\alpha\beta}), & (M_{\alpha 3}) \\ (M_{3\beta}), & (M_{33}) \end{bmatrix}, \tag{62}$$

so that the plate inertia associated with the displacements is expressed by $\omega^2 \mathbf{L} \cdot \mathbf{u}^0$.

Using the homogenized coefficients, the macroscopic (homogenized) plate equation (54)

satisfied by macroscopic functions $(p^0, g^0, \mathbf{u}^0, \boldsymbol{\theta}^0)$ can be rewritten, as follows

$$\begin{aligned}
& -\omega^2 \int_{\Gamma_0} \gamma^{-1} \left((\mathbf{L}\mathbf{u}^0) \cdot \mathbf{v} + \frac{h^2}{12} (\tilde{\mathcal{M}}\boldsymbol{\theta}^0) \cdot \boldsymbol{\vartheta} \right) + \int_{\Gamma_0} (\mathbf{S}^H(\bar{\nabla}_x u_3^0 - \boldsymbol{\theta}^0)) \cdot (\bar{\nabla}_x v_3 - \boldsymbol{\vartheta}) \\
& + \frac{h^2}{12} \int_{\Gamma_0} (\mathbb{E}^H \bar{\nabla}_x^S \boldsymbol{\theta}^0) : \bar{\nabla}_x^S \boldsymbol{\vartheta} + \int_{\Gamma_0} (\mathbb{E}^H \bar{\nabla}_x^S \bar{\mathbf{u}}^0) : \bar{\nabla}_x^S \bar{\mathbf{v}} \\
& - i\omega\rho_0 \int_{\Gamma_0} p^0 \mathbf{H} : \bar{\nabla}_x^S \bar{\mathbf{v}} - i\omega\gamma^{-1} \int_{\Gamma_0} \mathbf{v} \cdot (\mathbf{D}\bar{\nabla}p^0 + i\omega\mathbf{C}g^0) = 0,
\end{aligned} \tag{63}$$

recalling $\gamma^{-1} = \frac{\rho_0}{h}$.

3.4.2. Coupling conditions on Γ_0

This condition is necessary to close the system of equations describing the acoustic field p^ε in the transmission layer Ω_δ with the one describing the global acoustic field P^δ in Ω_δ^+ and Ω_δ^- . The following identity is a weak formulation of condition (12)₂,

$$\int_{\Gamma_\delta^+} \psi P^\delta - \int_{\Gamma_\delta^-} \psi P^\delta = \int_{\Gamma_0} \psi \int_{-\delta/2}^{\delta/2} \partial_{x_3} \tilde{p}^{\varepsilon\delta} \quad \forall \psi \in L^2(\Gamma_0), \tag{64}$$

where we assume $\psi = \psi(x')$, $x' \in \Gamma_0$; by $\tilde{\cdot}$ we denote an extension of $p^{\varepsilon\delta}$ to the whole Ω_δ . Further we proceed as in [9] by introducing an approximation for a finite layer thickness $\delta_0 = \varkappa\varepsilon_0 > 0$, such that (64) yields the following limit condition

$$\frac{1}{\varepsilon_0} \int_{\Gamma_0} \psi (\hat{P}^+ - \hat{P}^{t-}) = \int_{\Gamma_0} \psi \left(\int_{I_y^+} p^1 - \int_{I_y^-} p^1 \right) \quad \forall \psi \in L^2(\Gamma_0), \tag{65}$$

where $\hat{P}^{+/-}$ are the limit traces of P^δ on $\Gamma_\delta^{+/-}$ for $\delta \rightarrow 0$. Upon substituting there p^1 by the split form (30), we get

$$\int_{\Gamma_0} \psi (\mathbf{B}' \cdot \bar{\nabla}_x p^0 - i\omega F g^0 + i\omega \mathbf{C}' \cdot \mathbf{u}^0) = \frac{1}{\varepsilon_0} \int_{\Gamma_0} \psi (\Delta \hat{P}) \quad \forall \psi \in L^2(\Gamma_0). \tag{66}$$

where $\Delta \hat{P} = \hat{P}^+ - \hat{P}^+$ and

$$\begin{aligned}
F &= - \int_{I_y^+} \xi + \int_{I_y^-} \xi, \\
B'_\alpha &= \int_{I_y^+} \pi^\alpha - \int_{I_y^-} \pi^\alpha = \int_{Y_\varkappa^*} \partial_\alpha^y \xi = B_\alpha, \quad \alpha = 1, 2, \\
C'_k &= \int_{I_y^+} \eta^k - \int_{I_y^-} \eta^k = \int_{\partial S} n_k \xi = C_k, \quad k = 1, 2, 3.
\end{aligned} \tag{67}$$

In the next section, we shall formulate the global problem whose the solution describe the acoustic field in $\Omega^G = \hat{\Omega}^+ \cup \hat{\Omega}^- \cup \Gamma_0$. Acoustic waves in the homogenized fictitious layer

represented by Γ_0 with embedded perforated plate are governed by the system of equations (57), (63), and (66) expressing the transmission conditions involving the homogenized coefficients. This system is featured by some symmetries due to the following theorem.

Proposition 2.

(i) *Coefficients involved in the coupled transmission conditions (57), (63), and (66) satisfy the following relationships (recall $\alpha, \beta = 1, 2, k = 1, 2, 3$)*

$$\begin{aligned}
M_{\alpha\beta} &= M_{\beta\alpha}, & M_{3\beta} &= M_{\beta 3}, \\
D_{\alpha\beta} &= D_{\beta\alpha}^*, & D_{3\beta} &= D_{\beta 3}^*, \\
H_{\alpha\beta}^* &= H_{\beta\alpha} = H_{\alpha\beta}, \\
A_{\alpha\beta} &= A_{\beta\alpha}, \\
B_\alpha &= B'_\alpha, \\
C_k &= C'_k.
\end{aligned} \tag{68}$$

(ii) *Coefficients $\tilde{\mathcal{M}}, \mathbf{M}, \mathbf{D}, \mathbf{A}, \mathbf{C}, \mathbf{B}$ and F depend on ω , in general.*

(iii) *For z -symmetric cells Y , see Definition 1,*

$$C_\alpha = 0, \quad B_\alpha = 0, \quad D_{3\alpha} = 0 \text{ and also } M_{3\alpha} = 0, \quad \alpha, \beta = 1, 2. \tag{69}$$

(iv) *Moreover, for z -symmetric cells Y , coefficients $A_{\alpha\beta}$ and $D_{\alpha k}$ do not depend on ω .*

The proof of Proposition 2, assertions (i) and (ii), is given in Appendix B. Although the frequency is involved in the $\mathcal{T}_{i\omega}$ operator and, thereby, the characteristic responses of problems (33)-(36) should depend on ω , it may not be clear if the homogenized coefficients do depend on ω as well. Assertion (iii) is the direct consequence of Proposition (1); in the case of z -symmetric cells Y , $\hat{w}^\beta = \hat{w}^\alpha \equiv 0$ and the “reduced” local problems (39) and (40) do not involve ω , which yields assertion (iv).

4. Global problem with homogenized transmission layer

The acoustic wave propagation in the bulk Ω^G and in the homogenized layer Γ_0 is described in terms of the global acoustic pressure \hat{P} defined in subdomains $\hat{\Omega}^+$ and $\hat{\Omega}^-$, and in terms of $(p^0, \mathbf{u}^0, \theta^0)$ involved in equations (57), (63) and (66) governing the vibro-acoustic interaction in the layer embedding the perforated plate. These fields are coupled through the limit conditions arising from (12).

4.1. Coupling condition and problem formulation

We summarize the equations describing fields $(p^0, \mathbf{u}^0, \theta^0)$ defined in the homogenized layer represented by Γ_0 . Due to symmetries stated in Proposition 2, after some straightforward manipulations, the system of equations (57), (63) and (66) attains a symmetric form. From (57) we get

$$\begin{aligned} & \int_{\Gamma_0} (\mathbf{A} \bar{\nabla}_x p^0) \cdot \bar{\nabla}_x q^0 - \omega^2 \int_{\Gamma_0} \left(\frac{\zeta^*}{c^2} + \bar{h} \rho_0 K \right) p^0 q^0 \\ & + i\omega \int_{\Gamma_0} \left(q^0 \bar{h} \mathbf{H} : \bar{\nabla}_x^S \bar{\mathbf{u}}^0 + \bar{\nabla}_x q^0 \cdot \mathbf{D} \mathbf{u}^0 \right) + i\omega \int_{\Gamma_0} (g^0 \mathbf{B} \cdot \bar{\nabla}_x q^0 + q^0 \Delta G^1) = 0, \end{aligned} \quad (70)$$

for all $q \in H^1(\Gamma_0)$. Upon multiplication by $\gamma = \bar{h}/\rho_0$ in (63), it becomes

$$\begin{aligned} & -\omega^2 \int_{\Gamma_0} \left((\mathbf{L} \mathbf{u}^0) \cdot \mathbf{v} + \frac{h^2}{12} (\tilde{\mathcal{M}} \theta^0) \cdot \boldsymbol{\vartheta} \right) + \int_{\Gamma_0} \gamma (\mathbf{S}^H (\bar{\nabla}_x u_3^0 - \theta^0)) \cdot (\bar{\nabla}_x v_3 - \boldsymbol{\vartheta}) \\ & + \frac{\gamma h^2}{12} \int_{\Gamma_0} (\mathbb{E}^H \bar{\nabla}_x^S \theta^0) : \bar{\nabla}_x^S \boldsymbol{\vartheta} + \int_{\Gamma_0} \gamma (\mathbb{E}^H \bar{\nabla}_x^S \bar{\mathbf{u}}^0) : \bar{\nabla}_x^S \bar{\mathbf{v}} \\ & - i\omega \int_{\Gamma_0} \left(p^0 \bar{h} \mathbf{H} : \bar{\nabla}_x^S \bar{\mathbf{v}} + \mathbf{v} \cdot \mathbf{D} \bar{\nabla} p^0 \right) + \omega^2 \int_{\Gamma_0} \mathbf{v} \cdot \mathbf{C} g^0 = 0, \end{aligned} \quad (71)$$

for all $(\mathbf{u}^0, \theta^0) \in [H_0^1(\Gamma_0)]^5$. Finally, (66) multiplied by $-i\omega$ yields

$$\frac{i\omega}{\varepsilon_0} \int_{\Gamma_0} \psi(\Delta \hat{P}) - \int_{\Gamma_0} \psi (i\omega \mathbf{B}' \cdot \bar{\nabla}_x p^0 + \omega^2 F g^0 - \omega^2 \mathbf{C}' \cdot \mathbf{u}^0) = 0, \quad \forall \psi \in L^2(\Gamma_0). \quad (72)$$

In [9], we derived a Dirichlet-to-Neumann (DtN) operator which relates ΔP and p^0 , satisfying

$$\Delta P = \frac{1}{\varepsilon_0} \left(\hat{P}^+ - \hat{P}^- \right), \quad \text{and } p^0 = \frac{1}{2} \left(\hat{P}^+ + \hat{P}^- \right), \quad (73)$$

with the averaged momentum fluxes \hat{G}_0^\pm defined, as follows

$$\begin{aligned} \hat{G}_0^\pm(x') &= \frac{1}{|\Xi|} \int_{\Xi} (g^0(x') + \varepsilon_0 g^{1,\pm}(x', y')) dy' \\ &= g^0(x') + \varepsilon_0 G^{1,\pm}(x'), \quad \text{where } G^{1,\pm} = \frac{1}{|\Xi|} \int_{\Xi} g^{1,\pm}(x', y') dy'. \end{aligned} \quad (74)$$

Now, using \hat{G}_0^\pm , we can express g^0 and ΔG^1 involved in (57). It holds that

$$\begin{aligned} g^0 &\approx \frac{1}{2} \left(\hat{G}_0^+ + \hat{G}_0^- \right) = g^0 + \frac{\varepsilon_0}{2} (G^{1+} + G^{1-}), \\ \Delta G^1 &= \frac{1}{|\Xi|} \int_{\Xi} \Delta g^1(x', y') dy' = G^{1+} - G^{1-} = \frac{1}{\varepsilon_0} \left(\hat{G}_0^+ - \hat{G}_0^- \right). \end{aligned} \quad (75)$$

We may now introduce the global problem of acoustic field in a waveguide equipped with the perforated plate. By \mathcal{G} we refer the DtN operator defined in an implicit way, using the equations representing the homogenized layer (70)-(72) which together with (73) and (75) establish the mapping $\mathcal{G} : \hat{P} \mapsto \hat{G}_0^\pm$. In response to an incident wave with its amplitude \bar{p} , we find \hat{P} in Ω^G satisfying

$$\begin{aligned} c^2 \nabla^2 \hat{P} + \omega^2 \hat{P} &= 0 \quad \text{in } \hat{\Omega}^+ \cup \hat{\Omega}^- , \\ r i \omega c \hat{P} + c^2 \frac{\partial \hat{P}}{\partial n} &= s 2 i \omega c \bar{p} \quad \text{on } \partial_{\text{ext}} \Omega^G , \\ \text{interface condition:} & \end{aligned} \tag{76}$$

$$\begin{aligned} \frac{\partial \hat{P}^s}{\partial n^s} \Big|_{\Gamma_{\varepsilon_0}^s} &= s i \omega \hat{G}^s \quad \text{on } \Gamma_0 , \quad s = +, - , \\ \mathcal{G}(\hat{P}, \hat{G}_0^\pm) &= 0 \quad \text{on } \Gamma_0 , \end{aligned}$$

where $\Gamma_{\varepsilon_0}^s$, $s = +, -$ is the layer surface for a given $\varepsilon_0 > 0$, and n^\pm are the unit normal vector outward to $\hat{\Omega}_{\varepsilon_0}^\pm$. Furthermore, the constants $r, s \in \{0, 1\}$ and \bar{p} are defined to describe incident, reflected, or absorbed acoustic waves in the fluid, according to a selected part of the boundary.

4.2. Weak formulation of the global problem

For numerical simulations reported in the following section, we need the weak formulation of problem (76) with the DtN mapping introduced above, so that a computational algorithm based on the finite element method can be used. In what follows, we consider z -symmetric microstructures which arise naturally due to the transverse isotropy of the plate. By the consequence, see Proposition 2, (iii), some homogenized coefficients vanish. In this respect, we denote $\overline{\mathbf{D}} = (D_{\alpha\beta})$ and $\overline{\mathbf{M}} = (M_{\alpha\beta})$. We employ the following bilinear

forms involving the homogenized coefficients introduced in the preceding sections,

$$\begin{aligned}
\mathcal{A}(p, q) &= \int_{\Gamma_0} \mathbf{A} \bar{\nabla} p \cdot \bar{\nabla} q, \\
\mathcal{S}((w, \boldsymbol{\theta}), (v, \boldsymbol{\vartheta})) &= \frac{\bar{h}}{\rho_0} \int_{\Gamma_0} \mathbf{S}^H (\bar{\nabla} w - \boldsymbol{\theta}) \cdot \bar{\nabla} v - \boldsymbol{\vartheta}, \\
\mathcal{E}(\boldsymbol{\theta}, \boldsymbol{\vartheta}) &= \frac{\bar{h}}{\rho_0} \int_{\Gamma_0} \mathbb{E}^H \bar{\nabla}^S \boldsymbol{\theta} \cdot \bar{\nabla}^S \boldsymbol{\vartheta}, \\
\mathcal{F}(g, \psi) &= \int_{\Gamma_0} F g \cdot \psi, \\
\mathcal{H}(\bar{\mathbf{v}}, p) &= \bar{h} \int_{\Gamma_0} \mathbf{H} : \bar{\nabla}^S \bar{\mathbf{v}} \cdot p, \\
\mathcal{C}(u, \psi) &= \int_{\Gamma_0} C_3 u \cdot \psi, \\
\mathcal{K}(p, q) &= \int_{\Gamma_0} \left(\frac{\zeta^*}{c^2} + \rho_0 \bar{h} K \right) p \cdot q, \\
\mathcal{L}(\bar{\mathbf{u}}, \bar{\mathbf{v}}) &= \int_{\Gamma_0} (\bar{\mathbf{M}} + \tilde{\mathcal{M}}) \bar{\mathbf{u}} \cdot \bar{\mathbf{v}}, \\
\mathcal{M}(\boldsymbol{\theta}, \boldsymbol{\vartheta}) &= \int_{\Gamma_0} \tilde{\mathcal{M}} \boldsymbol{\theta} \cdot \boldsymbol{\vartheta}, \\
\mathcal{N}(u_3, v_3) &= \int_{\Gamma_0} M_{33} u_3 \cdot v_3, \\
\mathcal{D}(\bar{\mathbf{v}}, p) &= \int_{\Gamma_0} \bar{\mathbf{D}} \bar{\mathbf{v}} \cdot \bar{\nabla} p.
\end{aligned} \tag{77}$$

We obtain the weak formulation of (76) governing the global acoustic field $\hat{P} \in H^1(\hat{\Omega}^+ \cup \hat{\Omega}^-)$ which satisfies

$$\begin{aligned}
c^2 \int_{\hat{\Omega}^+ \cup \hat{\Omega}^-} \nabla \hat{P} \cdot \nabla Q - \omega^2 \int_{\hat{\Omega}^+ \cup \hat{\Omega}^-} \hat{P} Q + \int_{\partial_{\text{ext}} \Omega^G} r i \omega c \hat{P} Q \\
- i \omega c^2 \left(\int_{\Gamma_0} \hat{G}_0^+ \cdot Q^+ - \int_{\Gamma_0} \hat{G}_0^- \cdot Q^- \right) = \int_{\partial_{\text{ext}} \Omega^G} s i \omega c \bar{p} Q,
\end{aligned} \tag{78}$$

for all $Q \in H^1(\hat{\Omega}^+ \cup \hat{\Omega}^-)$, whereby Q^\pm denotes the trace of Q on $\partial \hat{\Omega}^\pm$.

The DtN operator involving functions $(\hat{P}^\pm, p^0, \bar{\mathbf{u}}) \in [L^2(\Gamma_0)]^2 \times H^1(\Gamma_0) \times [H_0^1(\Gamma_0)]^2$ and $(\hat{G}_0^\pm, u_3, \boldsymbol{\theta}) \in [L^2(\Gamma_0)]^2 \times H_0^1(\Gamma_0) \times [H_0^1(\Gamma_0)]^2$ is represented by the following equalities arising from (70)-(72), where we employ (73) and (75), so that we have

$$\begin{aligned}
\mathcal{A}(p^0, q) - \omega^2 \mathcal{K}(p^0, q) + i \omega (\mathcal{D}(\bar{\mathbf{u}}, q) + \mathcal{H}(\bar{\mathbf{u}}, q)) + \frac{i \omega}{\varepsilon_0} \int_{\Gamma_0} [\hat{G}_0^+ - \hat{G}_0^-] \cdot q = 0, \\
- i \omega (\mathcal{D}(\bar{\mathbf{v}}, p^0) + \mathcal{H}(\bar{\mathbf{v}}, p^0)) + \mathcal{E}(\bar{\mathbf{u}}, \bar{\mathbf{v}}) - \omega^2 \mathcal{L}(\bar{\mathbf{u}}, \bar{\mathbf{v}}) = 0,
\end{aligned} \tag{79}$$

for all $(q, \bar{\mathbf{v}}) \in H^1(\Gamma_0) \times [H_0^1(\Gamma_0)]^2$, and

$$\begin{aligned} \frac{\omega^2}{2} \mathcal{F}([\hat{G}_0^+ + \hat{G}_0^-], \psi) - \omega^2 \mathcal{C}(u_3, \psi) - \frac{i\omega}{\varepsilon_0} \int_{\Gamma_0} [\hat{P}^+ - \hat{P}^-] \cdot \psi = 0, \\ \frac{\omega^2}{2} \mathcal{C}([\hat{G}_0^+ + \hat{G}_0^-], v_3) - \omega^2 \left(\mathcal{N}(u_3, v_3) + \frac{h^2}{12} \mathcal{M}(\boldsymbol{\theta}, \boldsymbol{\vartheta}) \right) \\ + \mathcal{S}((u_3, \boldsymbol{\theta}), (v_3, \boldsymbol{\vartheta})) + \frac{h^2}{12} \mathcal{E}(\boldsymbol{\theta}, \boldsymbol{\vartheta}) = 0, \end{aligned} \quad (80)$$

for all $(\psi, v, \boldsymbol{\vartheta}) \in L^2(\Gamma_0) \times H_0^1(\Gamma_0) \times [H_0^1(\Gamma_0)]^2$. Recall the coupling equation (73),

$$\int_{\Gamma_0} 2p^0 - [\hat{P}^+ + \hat{P}^-] \cdot q = 0 \quad \forall q \in L^2(\Gamma_0). \quad (81)$$

Now we can state the main result of this section.

Global acoustic problem with the homogenized perforated plate. Given the incident acoustic wave represented by \bar{p} on Γ_{in} , find the acoustic potential \hat{P} defined in $\hat{\Omega}^G = \hat{\Omega}^+ \cup \hat{\Omega}^-$ and other functions $(p^0, \hat{G}_0^\pm, \mathbf{u}, \boldsymbol{\theta})$ defined on Γ_0 such that the variational equalities (78)-(81) hold.

5. Numerical implementation of the transmission conditions

In this section, we explain a finite-element based implementation of the homogenized layer model (79)-(81). Its coupling with the discretized problem of the acoustic waveguide is postponed in Section 6.

5.1. Discretized micro-problems

We shall describe a procedure of computing the homogenized coefficients involved in the model of the homogenized transmission layer. For this, both subparts of the computational cell Y are discretized by finite elements. Due to the specific geometry of the perforation, Y is z -symmetric with a cylindrical hole $Y^* \cap S$, see (4), positions of the discretization nodes in Ξ_S representing the plate are shifted positions of those on either of the surfaces $\partial_S^\pm Y = \{y = (y', z) \in Y \mid z = \pm \bar{h}/2\}$. Moreover, by virtue of the elliptic differential operators involved in $\mathcal{T}_{i\omega}$, see (32). We shall describe the discretized form of the micro-problems related to the acoustic fluid-structure interaction coupling the response in the solid plate inclusion Ξ_c with the fluid response in Y^* . The effective plate stiffness coefficients (60) are given by the characteristic stationary responses (51)-(53) of the plate matrix Ξ_m which are computed using a standard finite element discretization of the elliptic problems.

5.1.1. Problems related to the acoustic fluid-structure interaction

We introduce a generic form of the characteristic problems (33)-(36). We use the matrix notations, such that \mathbf{u} and \mathbf{p} represent the displacement field ϖ and pressure field η involved in problem (35), recalling $\gamma = \bar{h}/\rho^0$. For the other problems (33)-(35),

the correspondence with the characteristic response functions (the correctors) is obvious, see Tab. 1. The following self-explaining matrix notation is employed to introduce the discretized characteristic problems,

$$\begin{aligned}
\hat{b}_c(\hat{w}, \hat{v}) &\stackrel{\text{FEM}}{\approx} \mathbf{v}^T \mathbf{A} \mathbf{w} , \\
\int_{\Xi_c} \rho \hat{w} \cdot \hat{v} &\stackrel{\text{FEM}}{\approx} \mathbf{v}^T \mathbf{M} \mathbf{w} , \\
\int_{\Xi_c} \hat{w} \cdot \llbracket \hat{q} \rrbracket_h^\pm &\stackrel{\text{FEM}}{\approx} \mathbf{q}^T \mathbf{B} \mathbf{w} , \\
\int_{Y^*} \nabla_y \hat{p} \cdot \nabla_y \hat{q} &\stackrel{\text{FEM}}{\approx} \mathbf{q}^T \mathbf{C} \mathbf{p} ,
\end{aligned} \tag{82}$$

where \mathbf{w} and \mathbf{v} contain the displacement DOFs, whereas \mathbf{q} and \mathbf{p} represent the pressure DOFs. Further, the r.h.s. in problems (33)-(36) are approximated using vectors \mathbf{b} and \mathbf{r} , so that

$$\begin{aligned}
\int_{Y^*} \bar{\nabla}_y y_\alpha \cdot \bar{\nabla}_y q &\stackrel{\text{FEM}}{\approx} \mathbf{q}^T \bar{\mathbf{b}}_\alpha , \quad \bar{\mathbf{r}}_\alpha = \mathbf{0} , \\
\int_{I_y^+} q - \int_{I_y^-} q &\stackrel{\text{FEM}}{\approx} \mathbf{q}^T \mathbf{b}_\xi , \quad \mathbf{r}_\xi = \mathbf{0} , \\
\bar{h} \rho_0 \int_{\partial \Xi_S} n_\alpha \int_{-1/2}^{1/2} \xi &\stackrel{\text{FEM}}{\approx} \mathbf{q}^T \mathbf{b}_\alpha , \quad \mathbf{r}_\alpha = \mathbf{0} , \\
\int_{\Xi_S} \llbracket q \rrbracket_h^\pm \cdot 1 &\stackrel{\text{FEM}}{\approx} \mathbf{q}^T \mathbf{b}_3 , \quad \int_{\Xi_c} \rho \hat{v} \stackrel{\text{FEM}}{\approx} \hat{\mathbf{v}}^T \mathbf{r}_3 ,
\end{aligned} \tag{83}$$

Note that above the subscripts $_\alpha, \xi, _3$ are the labels and do not mean the vector component.

All problems (33)-(36) attain the following discretized form,

$$\underbrace{\begin{bmatrix} \gamma(\mathbf{A} - \omega^2 \mathbf{M}) , & -i\omega \mathbf{B}^T \\ i\omega \mathbf{B} , & \mathbf{C} \end{bmatrix}}_{\mathbf{K}} \underbrace{\begin{bmatrix} \mathbf{u} \\ \mathbf{p} \end{bmatrix}}_{\mathbf{q}} = - \underbrace{\begin{bmatrix} i\omega \gamma \mathbf{r} \\ \mathbf{b} \end{bmatrix}}_{\mathbf{f}} , \tag{84}$$

thus, $\mathbf{K} \mathbf{q} = -\mathbf{f}$. Obviously, matrix \mathbf{K} depending on ω can become singular for certain ω approaching resonances.

5.1.2. Solution procedure

We shall provide a computationally efficient method for robust computing the characteristic responses of problems (33)-(36) within any frequency range.

Let $\mathbf{v} = i\omega \mathbf{u}$, then (84) can be written as

$$\begin{bmatrix} \gamma \mathbf{D}_\omega , & \mathbf{B}^T \\ \mathbf{B} , & \mathbf{C} \end{bmatrix} \begin{bmatrix} \mathbf{v} \\ \mathbf{p} \end{bmatrix} = \begin{bmatrix} \gamma \mathbf{r} \\ -\mathbf{b} \end{bmatrix} \quad \text{with } \mathbf{D}_\omega = \omega^{-2} \mathbf{A} - \mathbf{M} . \tag{85}$$

It shows that both \mathbf{v} and \mathbf{p} are real column matrices, hence \mathbf{u} is purely imaginary. Further we consider the eigenvalues $\{\lambda_j\}$ and eigenvectors $\{\mathbf{w}^j\}$,

$$\mathbf{A}\mathbf{W} = \mathbf{M}\mathbf{W}\mathbf{\Lambda}, \quad \mathbf{W}^T\mathbf{M}\mathbf{W} = \mathbf{I}, \quad \mathbf{\Lambda} = \text{diag}(\lambda_j), \quad \mathbf{W} = [\mathbf{w}^1, \dots, \mathbf{w}^n], \quad (86)$$

so that \mathbf{W} is the modal matrix composed of eigenvectors \mathbf{w}^j associated with eigenvalues $\lambda^j \in \mathbb{R}$, $j = 1, \dots, n$, where n is the size and also the rank of matrix \mathbf{A} .

Using the modal transformation, $\mathbf{v} = \sum_{i=1}^n \mathbf{w}^i x_i = \mathbf{W}\mathbf{x}$, where $\mathbf{x} = (x_i)$, due to (86), problem (85) becomes

$$\begin{bmatrix} \gamma(\omega^{-2}\mathbf{\Lambda} - \mathbf{I}), & \mathbf{R}^T \\ \mathbf{R}, & \mathbf{C} \end{bmatrix} \begin{bmatrix} \mathbf{x} \\ \mathbf{p} \end{bmatrix} = \begin{bmatrix} \gamma\mathbf{W}^T\mathbf{r} \\ -\mathbf{b} \end{bmatrix}, \quad \text{with } \mathbf{R} = \mathbf{B}\mathbf{W}. \quad (87)$$

Thus, system matrix in (87) becomes singular near resonances $\omega^2 = \lambda_j$ for some $j = 1, \dots, n$.

As the next step, we express $\mathbf{p} = -\mathbf{C}^{-1}(\mathbf{R}\mathbf{x} + \mathbf{b})$ from (87)₂, which yields

$$\begin{aligned} \mathbf{G}\mathbf{x} &= -\mathbf{h}, \quad \text{with } \mathbf{G} = \mathbf{H} - \omega^{-2}\mathbf{\Lambda}, \\ \mathbf{H} &= \mathbf{I} + \gamma^{-1}\mathbf{R}^T\mathbf{C}^{-1}\mathbf{R}, \\ \mathbf{h} &= \mathbf{W}^T\mathbf{r} + \gamma^{-1}\mathbf{R}^T\mathbf{C}^{-1}\mathbf{b}. \end{aligned} \quad (88)$$

While \mathbf{H} is a regular matrix, \mathbf{G} can become singular because of the resonances. The eigenvalues $\{\epsilon_j\}$ and eigenvectors $\{\mathbf{z}^j\}$ of matrix \mathbf{H} satisfy

$$\mathbf{H}\mathbf{Z} = \mathbf{\Lambda}\mathbf{Z}\mathbf{E}, \quad \mathbf{Z}^T\mathbf{\Lambda}\mathbf{Z} = \mathbf{I}, \quad \mathbf{E} = \text{diag}(\epsilon_j), \quad \mathbf{Z} = [\mathbf{z}^1, \dots, \mathbf{z}^n], \quad (89)$$

The modal matrix \mathbf{Z} is composed of eigenvectors \mathbf{z}^j associated with eigenvalues $\eta^j \in \mathbb{R}$, $j = 1, \dots, n$, where n is the size of matrix \mathbf{H} . Using the modal transformation, $\mathbf{x} = \sum_{i=1}^n \mathbf{z}^i y_i = \mathbf{Z}\mathbf{y}$, where $\mathbf{y} = (y_i)$, problem (89) multiplied by \mathbf{Z}^T from the left becomes

$$\begin{aligned} \mathbf{Z}^T(\mathbf{H} - \omega^{-2}\mathbf{\Lambda})\mathbf{Z}\mathbf{y} &= -\mathbf{Z}^T\mathbf{h}, \\ \text{hence } \mathbf{y} &= -(\mathbf{E} - \omega^{-2}\mathbf{I})^{-1}\mathbf{Z}^T\mathbf{h} \\ &= \text{diag}\left(\frac{\omega^2}{1 - \omega^2\epsilon_j}\right)\mathbf{Z}^T\mathbf{h}. \end{aligned} \quad (90)$$

Using all the backward substitutions, the characteristic responses of (84) can be expressed, as follows

$$\begin{aligned} i\omega\mathbf{u} &= \mathbf{v} = \mathbf{W}\mathbf{x} = \mathbf{W}\mathbf{Z}\mathbf{y}, \\ \mathbf{p} &= -\mathbf{C}^{-1}(\mathbf{R}\mathbf{Z}\mathbf{y} + \mathbf{b}). \end{aligned} \quad (91)$$

Remark 1. Both the eigenvalue problems (86) and (89) are defined in terms of real symmetric positive definite matrices, so that eigenvalues λ_j and ϵ_j are real positive. The resonance effect $\omega^2 \rightarrow 1/\epsilon_j$ for any $j = 1, \dots, n$ depends on the spectral properties of

micro-problem	char. resp.	FE-discretized solutions	assoc. r.h.s. vectors	for z -symm. cells Y
(33)	$(\hat{w}^\beta, \pi^\beta)$	$(\mathbf{u}_\beta, \mathbf{p}_\beta)$	$\mathbf{0}, \bar{\mathbf{b}}_\beta$	$\bar{\mathbf{u}}_\beta \equiv \mathbf{0}$
(34)	$(\hat{\zeta}, \xi)$	$(\mathbf{u}_\xi, \mathbf{p}_\xi)$	$\mathbf{0}, \mathbf{b}_\xi$	
(35)	$(\hat{\omega}^\alpha, \eta^\alpha)$	$(\mathbf{u}_\alpha, \mathbf{p}_\alpha)$	$\mathbf{0}, \mathbf{b}_\alpha$	$\mathbf{u}_\alpha \equiv \mathbf{0}$
(36)	$(\hat{\omega}^3, \eta^3)$	$(\mathbf{u}_3, \mathbf{p}_3)$	$\mathbf{0}, \mathbf{b}_3$	

Table 1: Notation associated with microproblems (33)-(36). In the last column, the cancellations follow due to Proposition 2.

the matrices \mathbf{A} and \mathbf{C} by virtue of eigenvalues $\{\lambda_j\}$ and $\{\epsilon_j\}$, respectively; in the latter case, the projected inverse of \mathbf{C} is involved in the definition of matrix \mathbf{H} through the term $\mathbf{R}^T \mathbf{C}^{-1} \mathbf{R}$ which is of the same dimension, as \mathbf{A} .

To avoid computing of the inverse matrix \mathbf{C}^{-1} , the following problems are solved for matrix \mathbf{S} and vectors \mathbf{d}_s ,

$$\begin{aligned} \mathbf{C}\mathbf{S} &= \mathbf{R}, & \Rightarrow \mathbf{R}^T \mathbf{C}^{-1} \mathbf{R} &= \mathbf{R}^T \mathbf{S}, \\ \mathbf{C}\mathbf{d}_s &= \mathbf{b}_s, & \text{where } \mathbf{b}_s &\text{ is substituted by } \mathbf{b}_\alpha, \bar{\mathbf{b}}_\alpha, \mathbf{b}_\xi, \mathbf{b}_3. \end{aligned} \quad (92)$$

△

5.1.3. Homogenized coefficients

We shall now present formulae for computing the homogenized coefficients depending on the characteristic responses of microproblems (33)-(36) which all can be represented by the generic form of the microproblem (84) discretized by finite elements (FE). The homogenized coefficients are evaluated using matrix objects introduced in Tab. 1 associated with the formulae presented in Section 3.4.1 by virtue of the FE discretization. Vectors \mathbf{b}_s and \mathbf{r}_s , for index s understood in the context of Tab. 1, also constitute the r.h.s. vectors in the generic microproblem (84). Furthermore, according to (88) and using (92), we compute column vectors

$$\mathbf{h}_s = \mathbf{W}^T \mathbf{r}_s + \gamma^{-1} \mathbf{R}^T \mathbf{C}^{-1} \mathbf{b}_s = \mathbf{W}^T \mathbf{r}_s + \gamma^{-1} \mathbf{S}^T \mathbf{b}_s = \mathbf{W}^T \mathbf{r}_s + \gamma^{-1} \mathbf{R}^T \mathbf{d}_s, \quad (93)$$

which are involved in the expressions for \mathbf{u}_s .

Below we introduce in detail only the matrix expression of coefficient M_{33} , for the others the expressions are stated under the z -symmetry assumption which applies in the case of the plate perforations considered in the present study. For more general plate perforations, expressions of the homogenized coefficients are derived in Appendix C using the spectral matrix objects $\mathbf{Z} \text{diag}(\omega^2/1 - \omega^2 \epsilon_j) \mathbf{Z}^T$ and vectors \mathbf{b} and \mathbf{h} introduced in (83) and (88).

Coefficient \underline{M}_{33} . This coefficient depends on the mean plate density, $\bar{\rho}_S$, in particular $M_{33} = \bar{\rho}_S + \underline{M}_{33}(\omega)$, where \underline{M}_{33} is expressed by $(\hat{\omega}^3, \eta^3)$ being approximated by the couple

$(\mathbf{u}_3, \mathbf{p}_3)$. Using the discretized expressions (83)₄ we get

$$\begin{aligned}
\widetilde{M}_{33}(\omega) &= i\omega\gamma \int_{\Xi_c} \rho \widehat{\omega}^3 - \int_{\Xi_s} \llbracket \eta^3 \rrbracket_h^\pm \\
&\stackrel{\text{FEM}}{\approx} i\omega\gamma \mathbf{r}_3^T \mathbf{u}_3 - \mathbf{b}_3^T \mathbf{p}_3 = \gamma \mathbf{r}_3^T \mathbf{W} \mathbf{x} + \mathbf{b}_3^T \mathbf{C}^{-1} (\mathbf{R} \mathbf{x} + \mathbf{b}_3) \\
&= \gamma \mathbf{h}_3^T \mathbf{Z} \mathbf{y} + \mathbf{b}_3^T \mathbf{C}^{-1} \mathbf{b}_3 \\
&= \gamma \mathbf{h}_3^T \mathbf{Z} \operatorname{diag} \left(\frac{\omega^2}{1 - \omega^2 \epsilon_j} \right) \mathbf{Z}^T \mathbf{h}_3 + \mathbf{b}_3^T \mathbf{C}^{-1} \mathbf{b}_3,
\end{aligned} \tag{94}$$

$$\text{hence } M_{33} = \gamma \overline{\rho}_S + \mathbf{b}_3^T \mathbf{C}^{-1} \mathbf{b}_3 + \gamma \mathbf{h}_3^T \mathbf{Z} \operatorname{diag} \left(\frac{\omega^2}{1 - \omega^2 \epsilon_j} \right) \mathbf{Z}^T \mathbf{h}_3,$$

where \mathbf{x} and \mathbf{y} are associated to \mathbf{u} by virtue of (91).

For all other homogenized coefficients depending on characteristic responses (33)-(36) the expressions are derived in analogy with (94) using the \mathbf{b}_s and \mathbf{h}_s defined in (83) and (88), taking into account the z -symmetry property of cell Y . Hence, as the consequence of Lemma 1,

$$\begin{aligned}
\mathbf{b}_3^T \mathbf{p}_\beta &= \mathbf{0}, & \mathbf{b}_3^T \overline{\mathbf{p}}_\beta &= \mathbf{0}, \\
\mathbf{b}_\xi^T \mathbf{p}_\beta &= \mathbf{0}, & \mathbf{b}_\xi^T \overline{\mathbf{p}}_\beta &= \mathbf{0}.
\end{aligned} \tag{95}$$

Recalling Proposition 2, $\overline{\mathbf{u}}_\alpha$ and \mathbf{u}_α vanish, which is indicated consistently by vanishing projections

$$\mathbf{Z}^T \mathbf{b}_\alpha = \mathbf{0}, \quad \text{and} \quad \mathbf{Z}^T \overline{\mathbf{b}}_\alpha = \mathbf{0}. \tag{96}$$

By the consequence, expressions of some of the homogenized coefficients simplify. With reference to Proposition 2 (iii), we first present the nonvanishing coefficients,

$$\begin{aligned}
M_{\alpha\beta}(\omega) &= -\bar{h} \int_{\partial\Xi_S} n_\alpha \int_{-1/2}^{1/2} \eta^\beta d\zeta \stackrel{\text{FEM}}{\approx} -\mathbf{b}_\alpha^T \mathbf{p}_\beta = \mathbf{b}_\alpha^T \mathbf{C}^{-1} \overline{\mathbf{b}}_\beta, \\
D_{\alpha\beta} &= \bar{h} \int_{\partial\Xi_S} n_\alpha \int_{-1/2}^{1/2} \pi^\beta \stackrel{\text{FEM}}{\approx} -\mathbf{b}_\alpha^T \mathbf{C}^{-1} \overline{\mathbf{b}}_\beta, \\
C_3 &= \int_{\Xi_S} \llbracket \xi \rrbracket_h^\pm - i\omega\gamma \int_{\Xi_c} \rho_c \hat{\zeta} \stackrel{\text{FEM}}{\approx} -\mathbf{b}_3^T \mathbf{C}^{-1} \mathbf{b}_\xi - \gamma \mathbf{h}_3^T \mathbf{Z} \operatorname{diag} \left(\frac{\omega^2}{1 - \omega^2 \epsilon_j} \right) \mathbf{Z}^T \mathbf{h}_\xi, \\
F &= - \left(\int_{I_y^+} \xi - \int_{I_y^-} \xi \right) \stackrel{\text{FEM}}{\approx} \mathbf{b}_\xi^T \mathbf{C}^{-1} \mathbf{b}_\xi + \gamma \mathbf{h}_\xi^T \mathbf{Z} \operatorname{diag} \left(\frac{\omega^2}{1 - \omega^2 \epsilon_j} \right) \mathbf{Z}^T \mathbf{h}_\xi.
\end{aligned} \tag{97}$$

The acoustic propagation tensor $A_{\alpha\beta}$ is computed using the solution of problem (39). The generic discretized representation (84) involves $(\overline{\mathbf{u}}_\beta, \overline{\mathbf{p}}_\beta)$ as the approximations of $(\widehat{\omega}^\beta, \pi^\beta)$. Using the notation reported in (83) and \mathbf{h}_α evaluated according to (93), the following

expressions are obtained,

$$\begin{aligned}
A_{\alpha\beta} &= \int_{Y^*} \nabla_y(\pi^\beta + y_\beta) \cdot \nabla_y y_\alpha = \frac{|Y^*|}{|\Xi|} \delta_{\alpha\beta} + \tilde{A}_{\alpha\beta} , \\
\text{where } \tilde{A}_{\alpha\beta} &= \int_{Y^*} \bar{\nabla}_y y_\alpha \cdot \bar{\nabla}_y \pi^\beta \stackrel{\text{FEM}}{\approx} \bar{\mathbf{b}}_\alpha^T \bar{\mathbf{p}}_\beta \\
&= -\bar{\mathbf{b}}_\alpha^T \mathbf{C}^{-1} \bar{\mathbf{b}}_\beta - \gamma \bar{\mathbf{h}}_\alpha^T \mathbf{Z} \operatorname{diag} \left(\frac{\omega^2}{1 - \omega^2 \epsilon_j} \right) \mathbf{Z}^T \bar{\mathbf{h}}_\beta ,
\end{aligned} \tag{98}$$

hence the symmetry $A_{\alpha\beta} = A_{\beta\alpha}$ is confirmed.

Finally, the coefficients vanishing due to (95) and (96) are listed

$$\begin{aligned}
M_{3\beta}(\omega) &= i\omega\gamma \int_{\Xi_c} \rho \hat{\omega}^\beta - \int_{\Xi_s} \llbracket \eta^\beta \rrbracket_h^\pm \stackrel{\text{FEM}}{\approx} i\omega\gamma \mathbf{r}_3^T \mathbf{u}_\beta - \mathbf{b}_3^T \mathbf{p}_\beta = 0 , \\
D_{3\beta} &= \int_{\Xi_s} \llbracket \pi^\beta \rrbracket_h^\pm - i\omega\gamma \int_{\Xi_c} \rho_c \hat{w}^\beta \stackrel{\text{FEM}}{\approx} \mathbf{b}_3^T \bar{\mathbf{p}}_\beta - i\omega\gamma \mathbf{r}_3^T \bar{\mathbf{u}}_\beta = 0 , \\
C_\alpha &= \gamma \rho_0 \int_{\partial\Xi_s} n_\alpha \int_{-1/2}^{1/2} \xi \stackrel{\text{FEM}}{\approx} \mathbf{b}_\alpha^T \mathbf{p}_\xi = 0 , \\
B_\alpha &= \int_{Y^*} \bar{\nabla}_y y_\alpha \cdot \bar{\nabla}_y \xi \stackrel{\text{FEM}}{\approx} \bar{\mathbf{b}}_\alpha^T \mathbf{p}_\xi = 0 .
\end{aligned} \tag{99}$$

5.2. Macroscopic problem — matrix formulation

We consider a finite thickness $\delta_0 = \varepsilon_0 \varkappa$ of the transmission layer with $\varepsilon_0 > 0$ reflecting the size of the perforations. By the consequence, the global domain $\Omega_G^{\delta_0}$ splits into two parts $\Omega_+^{\delta_0}$ and $\Omega_-^{\delta_0}$ separated by the transmission layer Γ_{δ_0} which is represented by the homogenized transmission conditions (79)-(81) prescribed on Γ_0 . The acoustic field \hat{P}^\pm satisfying (78) is approximated by the 3D conforming P2 Lagrangian tetrahedral elements in $\Omega_G^{\delta_0}$. Accordingly, identic discretizations of interfaces $\Gamma_+^{\delta_0}$, $\Gamma_-^{\delta_0}$ and Γ_0 by triangular P2 elements are considered, so that condition (81) can be satisfied in the sense of the collocation at corresponding nodes. The fluxes g^0 and \hat{G}_0^\pm are approximated by P1 elements on the matching triangular mesh. As for the plated displacements \mathbf{u} and rotations $\boldsymbol{\theta}$ on Γ_0 , these are approximated by P2 elements and P1 elements, respectively. The vectors containing the nodal DOFs associated with discretised fields are designated in the following table:

vector / DOFs	approximated field	FE type
\mathbf{p}^\pm	\hat{P}^\pm , pressure traces on Γ_0^\pm	P2
\mathbf{g}^\pm	\hat{G}^\pm , acoustic momentum fluxes on Γ_0^\pm	P1
\mathbf{p}^0	p^0 , mean acoustic pressure on Γ_0	P2
\mathbf{g}^0	g^0 , mean acoustic momentum flux on Γ_0	P1
$\bar{\mathbf{u}}$	u_3 , deflections on Γ_0	P2
\mathbf{w}	$\boldsymbol{\theta}$, rotations on Γ_0	P1

5.2.1. FE discretized formulation of the transmission conditions

The FE-discretization of (79)-(81) leads to a matrix formulation involving the global vector of unknowns. Two alternatives can be used

$$\begin{aligned} \bar{\mathbf{q}} &= [\mathbf{p}^\pm; \mathbf{g}^\pm; \mathbf{u}; \mathbf{w}], \quad \text{with } \mathbf{u} = [\bar{\mathbf{u}}; \hat{\mathbf{u}}], \\ \text{or } \mathbf{q} &= [\mathbf{p}^0; \mathbf{g}^0; \mathbf{u}; \mathbf{w}]. \end{aligned} \quad (100)$$

where the Matlab notation “;” means the “line break”, thus, \mathbf{q} is the column vector.

To express p^0 and g^0 , nodal (collocation at FE nodes) operations are introduced,

$$\mathbf{g}^0 = \mathbf{X}\mathbf{g}^\pm, \quad \mathbf{p}^0 = \mathbf{X}\mathbf{p}^\pm, \quad (101)$$

whereas the jumps are expressed reciprocally (collocation at FE nodes),

$$\Delta G^1 \stackrel{\text{FEM}}{\approx} \mathbf{Z}_\varepsilon \mathbf{g}^\pm, \quad \Delta \hat{P}^\pm = \mathbf{Z}_\varepsilon \mathbf{p}^\pm, \quad (102)$$

where \mathbf{Z}_ε involves ε^{-1} , the (finite) scale, see (73) and (75). When approximating the DtN operator given in its implicit form by (79)-(81), the following matrix expressions of the discretized bilinear forms hold,

$$\begin{aligned} \mathcal{A}(p^0, q^0) &\stackrel{\text{FEM}}{\approx} (\mathbf{p}^0)^T \mathbf{A} \mathbf{q}^0, \quad \mathcal{K}(p^0, q^0) \stackrel{\text{FEM}}{\approx} (\mathbf{p}^0)^T \mathbf{Q} \mathbf{q}^0, \\ \mathcal{E}(\boldsymbol{\theta}, \boldsymbol{\vartheta}) &\stackrel{\text{FEM}}{\approx} \mathbf{t}^T \mathbf{E} \mathbf{w}, \quad \mathcal{M}(\boldsymbol{\theta}, \boldsymbol{\vartheta}) \stackrel{\text{FEM}}{\approx} \mathbf{t}^T \mathbf{T} \mathbf{w}, \\ \mathcal{H}(\bar{\mathbf{u}}, p^0) + \mathcal{D}(\bar{\mathbf{u}}, p^0) &\stackrel{\text{FEM}}{\approx} (\mathbf{p}^0)^T \mathbf{D} \bar{\mathbf{u}}, \quad \int_{\Gamma_0} g^0 \cdot p^0 \stackrel{\text{FEM}}{\approx} (\mathbf{p}^0)^T \mathbf{J} \mathbf{g}^0 \\ \mathcal{C}(u_3, g^0) &\stackrel{\text{FEM}}{\approx} (\mathbf{g}^0)^T \mathbf{C} \hat{\mathbf{u}}, \quad \mathcal{F}(g^0, \tilde{g}) \stackrel{\text{FEM}}{\approx} \tilde{\mathbf{g}}^T \mathbf{F} \mathbf{g}^0, \\ \mathcal{L}(\bar{\mathbf{u}}, \bar{\mathbf{v}}) &\stackrel{\text{FEM}}{\approx} \bar{\mathbf{v}}^T \mathbf{L} \bar{\mathbf{u}}, \quad \mathcal{N}(u_3, v_3) \stackrel{\text{FEM}}{\approx} \hat{\mathbf{V}}^T \mathbf{N} \hat{\mathbf{u}}. \end{aligned} \quad (103)$$

Matrix \mathbf{J} represents the scalar products (products of P2 and P1 functions of the FE partitioning, in our case)

$$\int_{\Gamma_0} \psi(\Delta \hat{P}), \quad \text{and} \quad \int_{\Gamma_0} q^0 \Delta G^1. \quad (104)$$

The shear-rotation coupling in the bilinear form \mathcal{S} yields the following discretized representation,

$$\mathcal{S}((u_3, \boldsymbol{\theta}), (v_3, \boldsymbol{\vartheta})) \stackrel{\text{FEM}}{\approx} [\bar{\mathbf{v}}; \hat{\mathbf{v}}; \mathbf{t}]^T \begin{bmatrix} \mathbf{0} & \mathbf{0} & \mathbf{0} \\ \mathbf{0} & \mathbf{S} & \mathbf{R} \\ \mathbf{0} & \mathbf{R}^T & \mathbf{0} \end{bmatrix} \begin{bmatrix} \bar{\mathbf{u}} \\ \hat{\mathbf{u}} \\ \mathbf{w} \end{bmatrix}. \quad (105)$$

Further we employ the stiffness and the mass matrices, denoted by \mathbf{K} and \mathbf{M} , respectively,

$$\mathbf{K} = \begin{bmatrix} \mathbf{E} & \mathbf{0} \\ \mathbf{0} & \mathbf{S} \end{bmatrix}, \quad \mathbf{M} = \begin{bmatrix} \mathbf{L} & \mathbf{0} \\ \mathbf{0} & \mathbf{N} \end{bmatrix}, \quad (106)$$

which enable to express the strain and kinetic energies of the plate denoted by E_S and E_K , respectively, being associated with the harmonic wave propagation,

$$\begin{aligned} E_S &= \frac{h}{2} [\mathbf{u}; \mathbf{w}]^T \begin{bmatrix} \mathbf{K} & -\mathbf{R} \\ -\mathbf{R}^T & \frac{h^2}{12} \mathbf{E} \end{bmatrix} [\mathbf{u}; \mathbf{w}] , \\ E_K &= -\omega^2 \frac{h}{2} [\mathbf{u}; \mathbf{w}]^T \begin{bmatrix} \mathbf{M} & \mathbf{0} \\ \mathbf{0} & \frac{h^2}{12} \mathbf{T} \end{bmatrix} [\mathbf{u}; \mathbf{w}] . \end{aligned} \quad (107)$$

Thus, matrix \mathbf{K} expresses the stiffness w.r.t. the displacements, *i.e.* involving the Young and the shear moduli, whereas matrix \mathbf{M} describes the frequency-dependent mass associated with plate displacements. Note that the elastic and kinetic energies depend also on the rotation.

Using a self-explaining notation, the system (70)-(72) is represented by the following matrix equation,

$$\bar{\mathbf{H}} \bar{\mathbf{q}} = \mathbf{0} , \quad (108)$$

where

$$\bar{\mathbf{H}} = \begin{bmatrix} \mathbf{X}^T (\mathbf{A} - \omega^2 \mathbf{Q}) \mathbf{X} & -i\omega \mathbf{X}^T \mathbf{J} \mathbf{Z}_\varepsilon & i\omega \mathbf{X}^T \mathbf{D} & \mathbf{0} \\ i\omega \mathbf{Z}_\varepsilon^T \mathbf{J} \mathbf{X} & -\omega^2 \mathbf{X}^T \mathbf{F} \mathbf{X} & \omega^2 \mathbf{X}^T \mathbf{C} & \mathbf{0} \\ -i\omega \mathbf{D}^T \mathbf{X} & \omega^2 \mathbf{C}^T \mathbf{X} & \mathbf{K} - \omega^2 \mathbf{M} & -\mathbf{R} \\ \mathbf{0} & \mathbf{0} & -\mathbf{R}^T & \frac{h^2}{12} (\mathbf{E} - \omega^2 \mathbf{T}) \end{bmatrix} .$$

is Hermitean matrix. Recalling Proposition 2, matrices \mathbf{M} , \mathbf{T} , \mathbf{C} and \mathbf{F} depend on the frequency ω and are affected by “micro-level” resonances through the homogenized coefficients;; in the case of \mathbf{M} , these resonances are associated with (90) through coefficients M_{kl} , see (94) and (97)₁, and also with the resonances featuring coefficients $\tilde{\mathcal{M}}_{\alpha\beta}$, see (59).

6. Numerical examples

This section with numerical examples is divided into two parts. The aim of the first part is to compare the results calculated by the newly derived model and by the previously published vibroacoustic model, see [9]. Our new model of the vibroacoustic transmission involves frequency-dependent homogenized coefficients and will be further referred to as the *metamaterial model*. The model published and validated in [9] will be denoted as a *standard model*. In the second part of this section, we demonstrate the microstructure with a modified inclusion, with which we can effectively change the distribution of resonant frequencies.

The presented numerical simulations are base on the discretization by means of the finite element method and have been implemented in *SfePy* – Simple Finite Elements in Python [33].

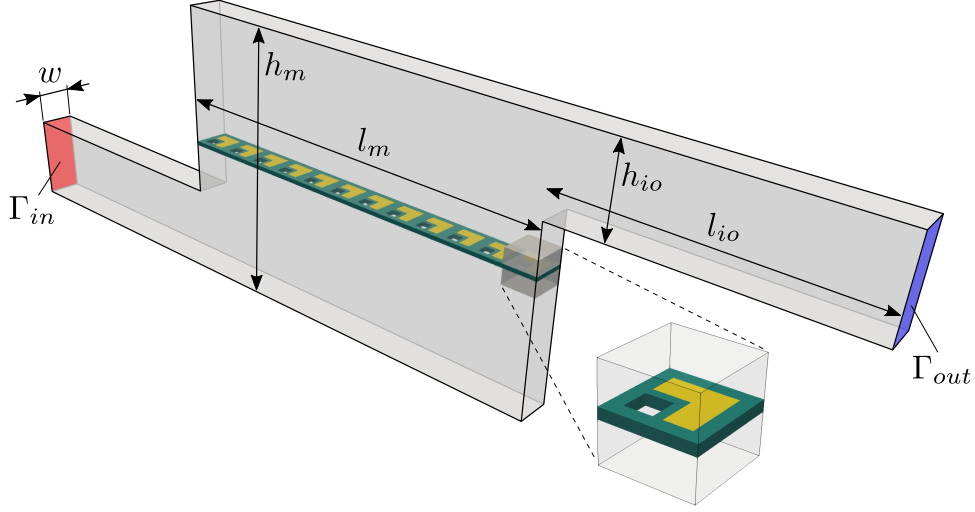


Figure 5: The acoustic domain with the embedded perforated elastic plate and the detailed view of the perforation.

6.1. Wave propagation in a waveguide

We consider the waveguide which domain is divided by the perforated plate into two parts of the same shape and size as illustrated in Fig. 5. The waveguide dimensions are the following: $l_m = 0.3$ m, $h_m = l_{io} = 0.2$ m, $h_{io} = 0.0625$ m and $w = 0.01$ m.

The computational domains $\hat{\Omega}^+$, $\hat{\Omega}^-$ and Γ_0 , employed for the numerical simulations of the acoustic transmission, are depicted in Fig. 6. The waveguide input is labelled as Γ_{in} and an incident wave is imposed on this part of the boundary. This condition is respected in (10) by values $r = s = 1$ and the amplitude of the incident wave, appearing in (10), is assumed to be $\bar{p} = 30$ Pa. At the waveguide output Γ_{out} , we consider the anechoic condition achieved by choosing $r = 1$, $s = 0$ in (10) on surface Γ_{out} . The elastic plate is fixed at the edges parallel to the x_2 -axis, see Fig. 6, such that $\bar{\mathbf{u}} = \mathbf{0}$, $w_3 = 0$ and $\boldsymbol{\theta} = \mathbf{0}$. The periodic boundary conditions are applied on the faces orthogonal to the x_2 -axis. This requirement leads to the homogeneous distribution of the macroscopic fields in the x_2 -direction.

The characteristic responses and the homogenized coefficients are calculated within the representative cells Y and Ξ , see Fig. 7. The 3D computational domain Y consists of the fluid domain Y^* , the elastic matrix S_m and the elastic inclusion S_c . In the similar way, the 2D plate domain Ξ comprises the matrix and inclusion parts Ξ_m and Ξ_c . The acoustic fluid is characterized by its density $\rho_0 = 1.55$ kg m³ and by the sound speed $c = 343$ m s⁻¹. We consider the aluminium matrix with the density $\rho_m = 2700$ kg m³, Young modulus $E_m = 70$ GPa and Poisson ratio $\nu_m = 0.34$. In order to obtain the contrast in the elasticity of the constituents, we employ the rubber inclusion with material parameters $\rho_c = 1200$ kg m³, $E_c^\varepsilon = 0.1$ GPa, thus $E_c = E_c^\varepsilon/\varepsilon^2$, and $\nu_c = 0.48$. The scaling parameter ε defining the size of the holes and elastic inclusions is chosen as $\varepsilon = 0.01$, which means that the thickness of the plate is $h^\varepsilon = \bar{h}\varepsilon$ for $\bar{h} = 0.12$.

Computational analysis of the resonant frequencies of subproblems (41) and (33)–(36)

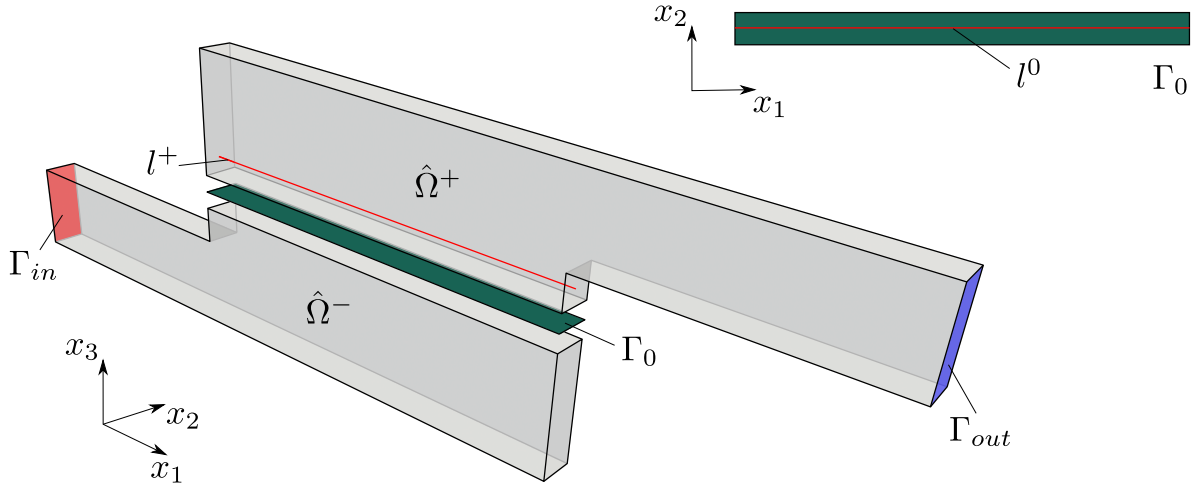


Figure 6: The computational domains $\hat{\Omega}^+$, $\hat{\Omega}^-$, Γ_0 employed in the numerical simulations of the acoustic transmission at the global (macroscopic) level.

results in the values presented in Tab. 2 and Tab. 3, where only the first six lowest frequencies for each subproblem are displayed.

$$\omega^{cfI} = \sqrt{\lambda} \text{ [Hz]} \parallel 246051 \mid 263714 \mid 274403 \mid 301639 \mid 326247 \mid 351988$$

Table 2: Critical frequencies related to problem (41), where λ are problem eigenvalues, see (43).

$$\omega^{cfII} = \sqrt{1/\epsilon} \text{ [Hz]} \parallel 36035 \mid 47332 \mid 54616 \mid 67843 \mid 68262 \mid 77368$$

Table 3: Critical frequencies related to problems (33)–(36), where ϵ are eigenvalues calculated according to (89).

In the following part, we compare the responses of the proposed model, which involves the frequency varying homogenized coefficients, with those obtained by the vibroacoustic model with frequency independent coefficients published in [9]. According to the notation discussed in the beginning of this section, the calculated values are labelled by superscripts mm (metamaterial model) and sm (standard model). We assume the frequency range 33 KHz – 57 KHz, involving the first three critical frequencies of problems (33)–(36). In Fig. 8 we plot the frequency dependent homogenized coefficients F , C_3 , M_{33} and the constant values of these coefficients obtained by the standard model. To compare a global (macroscopic) response of the models, we calculate the transmission loss TL employing the following expression:

$$\text{TL} = 10 \log_{10} \frac{\int_{\Gamma_{in}} |p|^2}{\int_{\Gamma_{out}} |p|^2}.$$

The TL values for the metamaterial and the standard models around the resonant frequency ω_1^{cfII} are shown in Fig. 9.

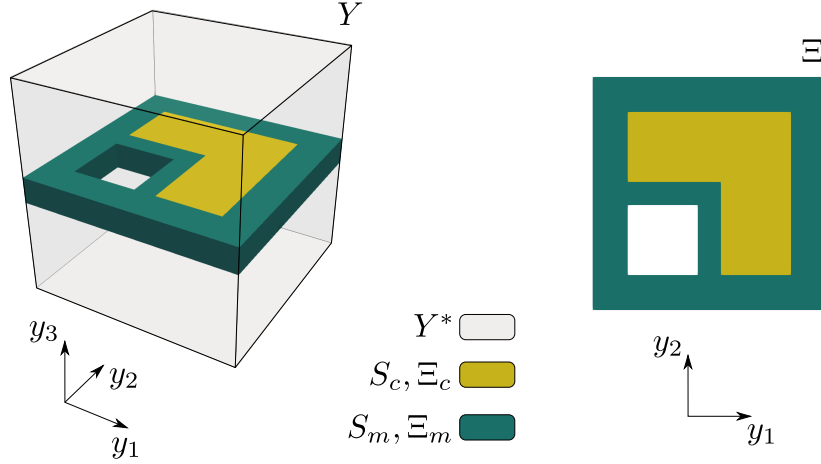


Figure 7: The computational domains Y and Ξ involved in the calculations of the characteristic responses and the homogenized coefficients.

Another comparison is made in Fig. 10, where we compare the results of both the models along the line probes l^+ and l^0 which are parallel to x_1 -axis and their positions are marked out in Fig. 6. Further, we choose three frequencies $\omega_1 = 33000$ Hz, $\omega_2 = 35900$ Hz and $\omega_3 = 36200$ Hz; the first one is far enough from the lowest critical frequency $\omega_1^{cfII} = 36035$ Hz, see Tab. 3, the second frequency is slightly lower ($\omega_1^{cfII} - \omega_2 = 135$ Hz) and the third one is slightly higher ($\omega_3 - \omega_1^{cfII} = 165$ Hz) than ω_1^{cfII} . The right bottom subfigure of Fig. 10 shows the acoustic pressures along the probe line l^+ calculated by the metamaterial model for $\omega_1, \omega_2, \omega_3$. The other subfigures compare the results p^{mm} obtained by the newly proposed model with the reference values p^{sm} . The distributions of the local acoustic pressure for given frequencies are depicted in Fig. 11. As for the acoustic pressure field, the similar comparisons for the plate deflection (transversal displacement) in Γ_0 are presented in Fig. 12 and Fig. 13. For the out-of-resonance frequency the standard and the metamaterial models provides the similar results as expected. Near resonance, the macroscopic fields of the metamaterial model are affected by varying homogenized coefficients so that they are either attenuated or amplified.

For illustration of the microscopic characteristic responses, we show the corrector functions $\pi^\beta, \xi, \hat{\zeta}$, see the local problems (33) and (34), calculated in the fluid domain Y^* and in the elastic inclusion Ξ_c .

6.2. Tuning of resonant frequencies

In the case of the metamaterial model, the critical frequencies are dependent on the geometrical arrangement of the perforated structure and on the material properties of the constituents. To demonstrate the effect of varying material parameters, we modify the soft inclusion (domain S_c) by an embedded part, see the left subfigure of Fig. 15, the specific weight and stiffness of which we parametrize as follows: $E_r = E_c \cdot k_r$ and $\rho_r = \rho_c \cdot k_r$. The dependence of the first few critical frequencies ω^{cfI} and ω^{cfII} on k_r is shown in Fig. 15

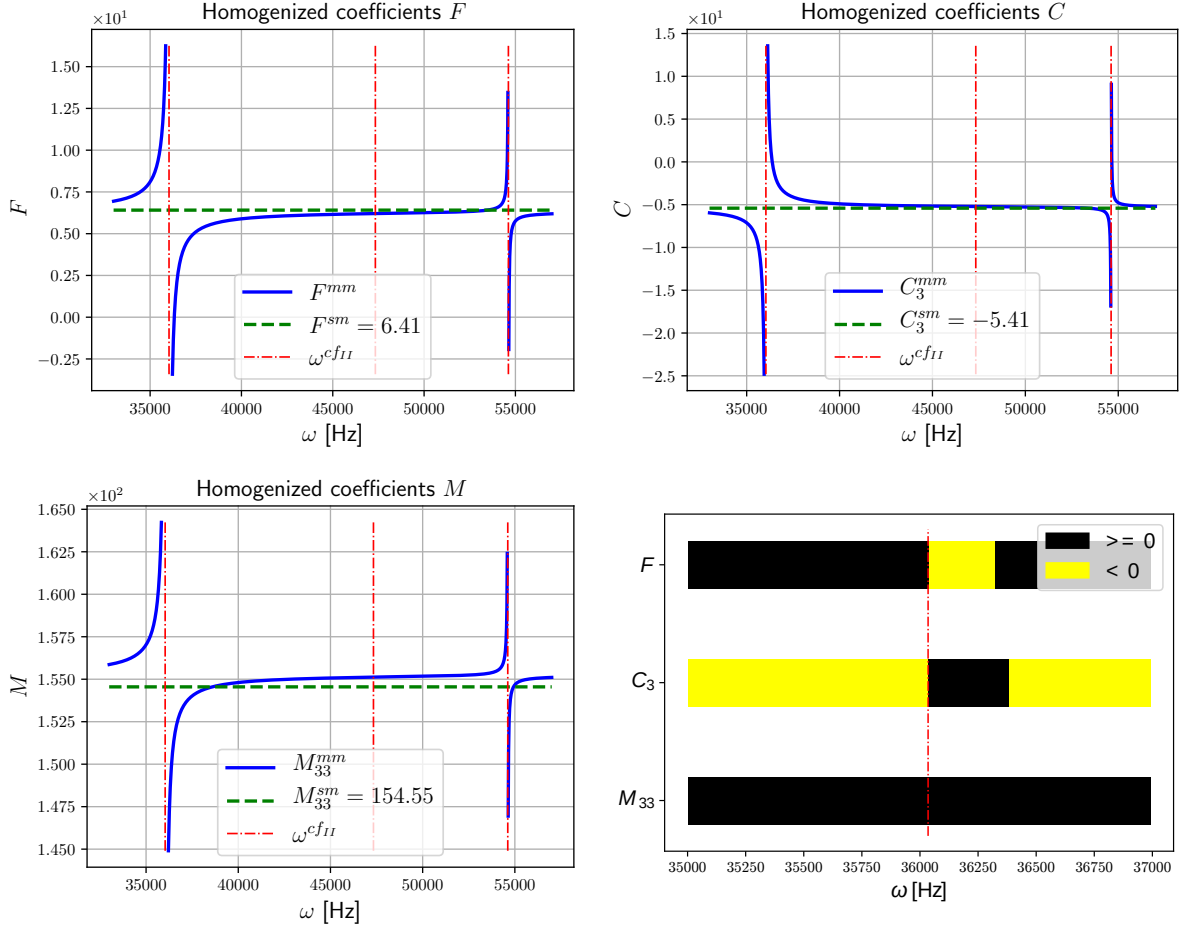


Figure 8: The frequency dependent homogenized coefficients F , C_3 and M_{33} calculated for the frequency range 33 KHz – 57 KHz.

right. We observe the significant drop of ω_1^{cfI} , ω_2^{cfI} and a slight decrease of ω_1^{cfII} , ω_2^{cfII} with increasing k_r , while the higher critical frequencies, e.g. ω_9^{cfII} , ω_{10}^{cfII} , increase.

Let $k_r = 19$, then we get the mingled critical frequencies ω^{cfI} and ω^{cfII} starting from $\omega = 93577$ Hz, see Fig. 16 left. Among these higher frequencies we are able to locate a range, where at least one eigenvalue of coefficient \tilde{M} is negative and also M_{33} is less than zero as depicted in Fig. 16 right. This indicates a possible band gap effects in a given frequency range.

7. Conclusion

We derived vibro-acoustic transmission conditions describing the interaction between the metamaterial plate and the surrounding acoustic fluid. The plate with periodic distribution of soft inclusions has been treated as the large contrast elastic medium with the scale-dependent stiffness of the resonators, following the idea of [29]. Due to this, the homogenization and the “3D to 2D” dimensional reduction enable to replace the 3D

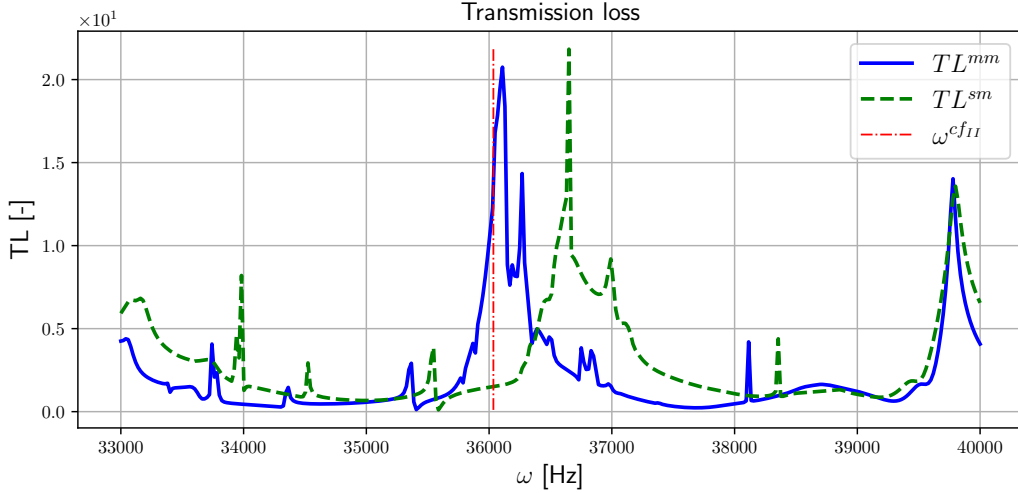


Figure 9: The transmission loss curves calculated by the metamaterial (TL^{mm}) and standard (TL^{sm}) models.

problem imposed in the transmission layer with a complicated geometry by the Dirichlet-to-Neumann operator given in an implicit form representing the metasurface. Frequency dependent effective coefficients of the homogenized model can be evaluated for thousands of frequencies in a time slot of seconds due to a very efficient algorithm based on a spectral decomposition of the representative periodic cell response. The numerical examples are rather illustrative, although they show some effects of the metamaterial plate model – in a neighbourhood of the resonance frequencies associated with the spectral decomposition of the fluid-structure interaction, the impedance and some other coefficients can change their signs which affects the acoustic transmission and the plate vibrations. Such a behaviour cannot be captured by the standard model [9], derived without the scale-related contrast property. Suitable design modifications (the size of holes, mechanical properties of the resonators) enable that all coefficients representing the metasurface mass density can become negative at least in narrow frequency intervals, thus, yielding the band gaps in the wave transmission. This motivates the further research towards optimized microstructures using the shape [34, 35], or topology [36] optimization up to now considered for the standard perforated plates. Further perspectives involve effects of flows through the perforated metamaterial plates and wave scattering in cascades of blades, *cf.* [37], or porous layered (sandwich) structures [38, 39] introducing naturally the attenuation.

Acknowledgment. The research at the University of West Bohemia has been supported by the grant project GACR 19-04956S of the Czech Scientific Foundation. and in a part due to the European Regional Development Fund-Project “Application of Modern Technologies in Medicine and Industry” (No. CZ.02.1.01/0.0/ 0.0/17 048/0007280) provided by the Czech Ministry of Education, Youth and Sports.

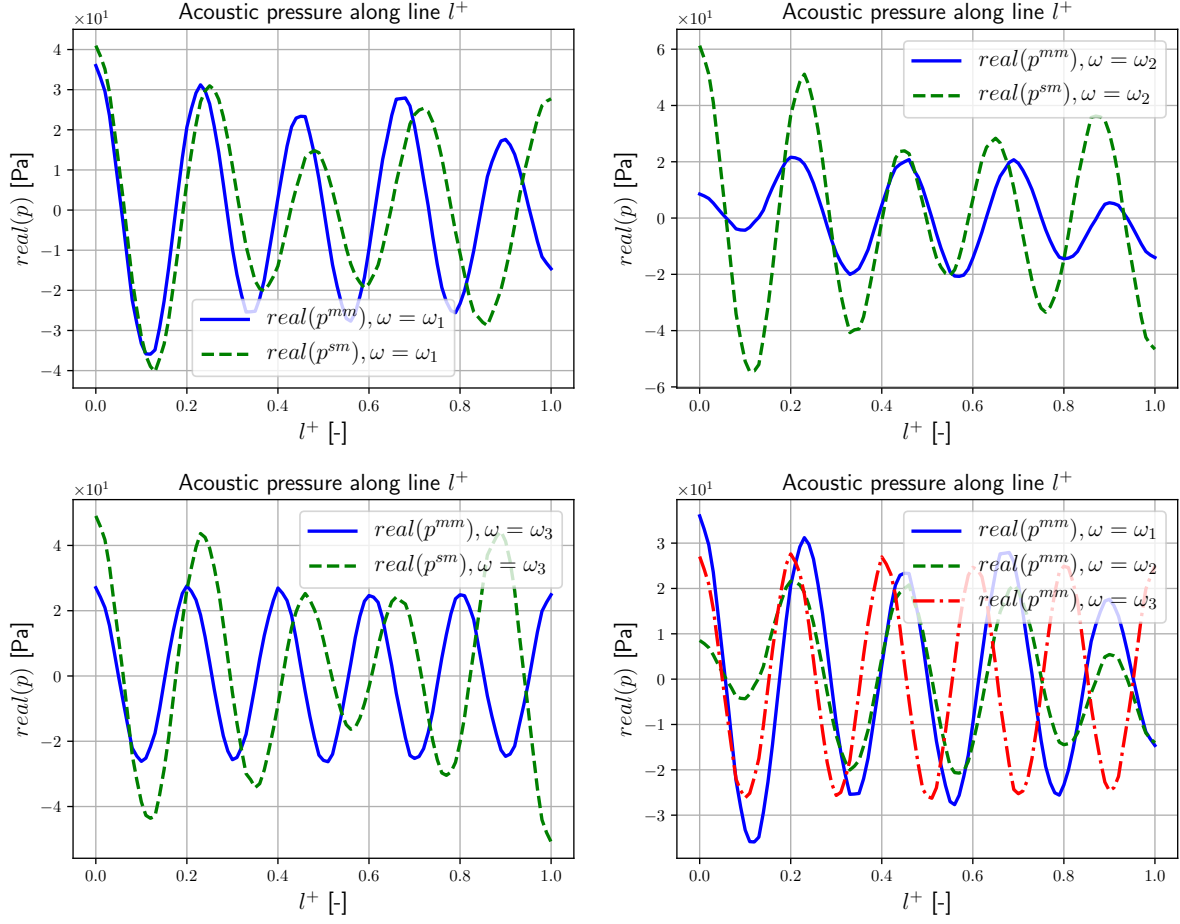


Figure 10: Comparison of the acoustic pressures calculated by the standard (p^{sm}) and the metamaterial (p^{mm}) models. The real parts of the pressure are plotted along line l^+ for frequencies $\omega_1 = 33000$ Hz, $\omega_2 = 35900$ Hz and $\omega_3 = 36200$ Hz.

Appendix A. Limit of the unfolded vibroacoustic problem

Upon unfolding the fluid equation (19), its l.h.s. yields the limit

$$\begin{aligned}
& c^2 \int_{\Gamma_0} \int_{Y^*} \mathcal{T}_\varepsilon(\overline{\nabla} p^\varepsilon) \cdot \mathcal{T}_\varepsilon(\overline{\nabla} q^\varepsilon) + \frac{c^2}{\varepsilon^2} \int_{\Gamma_0} \int_{Y^*} \partial_z \mathcal{T}_\varepsilon(p^\varepsilon) \partial_z \mathcal{T}_\varepsilon(q^\varepsilon) - \omega^2 \int_{\Gamma_0} \int_{Y^*} \mathcal{T}_\varepsilon(p^\varepsilon) \mathcal{T}_\varepsilon(q^\varepsilon) \\
\rightarrow & c^2 \int_{\Gamma_0} \int_{Y^*} (\overline{\nabla}_x p^0 + \overline{\nabla}_y p^1) \cdot (\overline{\nabla}_x q^0 + \overline{\nabla}_y q^1) + c^2 \int_{\Gamma_0} \int_{Y^*} \partial_z p^1 \partial_z q^1 - \omega^2 \int_{\Gamma_0} \int_{Y^*} p^0 q^0.
\end{aligned} \tag{A.1}$$

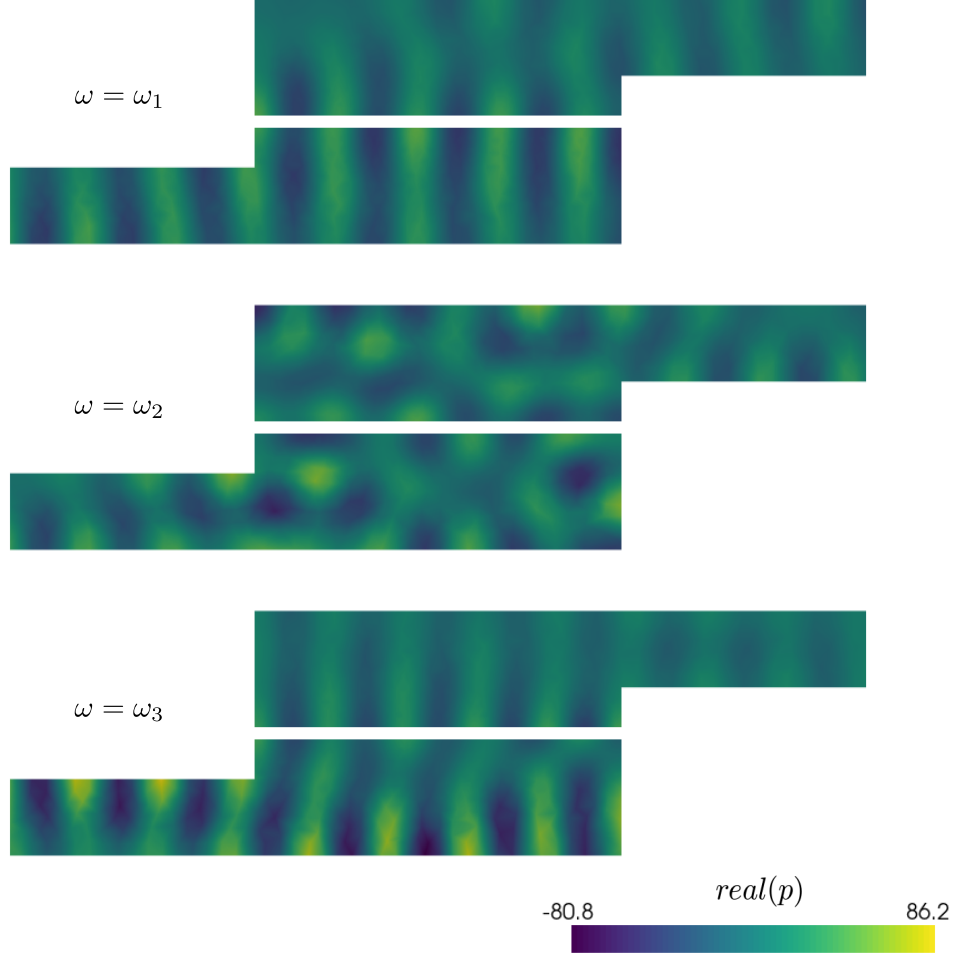


Figure 11: The distribution of the acoustic pressure (real part of p^{mm}) in the macroscopic domain $\hat{\Omega}^+ \cup \hat{\Omega}^-$.

The unfolded r.h.s. interaction terms in (19), below divided by $i\omega c^2$,

$$\begin{aligned}
& \frac{1}{\varepsilon} \int_{\Gamma_0} \int_{\Xi_S} (u_3^0 + \varepsilon u_3^1 + \chi_c \hat{u}_3) \varepsilon \llbracket q^1 \rrbracket_{\bar{h}}^\pm \\
& + \frac{\bar{h}}{\varepsilon} \int_{\Gamma_0} \int_{\partial \Xi_S} \int_{-1/2}^{1/2} \bar{\mathbf{n}} \cdot \left(\bar{\mathbf{u}}^0 + \varepsilon \bar{\mathbf{u}}^1 + \chi_c \hat{\bar{\mathbf{u}}} - \varepsilon \bar{h} \zeta (\boldsymbol{\theta}^0 + \varepsilon \boldsymbol{\theta}^1 + \chi_c \hat{\boldsymbol{\theta}}) \right) (q^0 + \varepsilon q^1),
\end{aligned} \tag{A.2}$$

converge, as follows:

$$\int_{\Gamma_0} \left(u_3^0 \int_{\Xi_S} \llbracket q^1 \rrbracket_{\bar{h}}^\pm + \bar{\mathbf{u}}^0 \cdot \int_{\partial \Xi_S} \bar{\mathbf{n}} \bar{h} \int_{-1/2}^{1/2} q^1 d\zeta + q^0 \bar{h} \int_{\partial \Xi_S} \bar{\mathbf{n}} \cdot \bar{\mathbf{u}}^1 + \int_{\Xi_c} \hat{u}_3 \llbracket q^1 \rrbracket_{\bar{h}}^\pm \right) \tag{A.3}$$

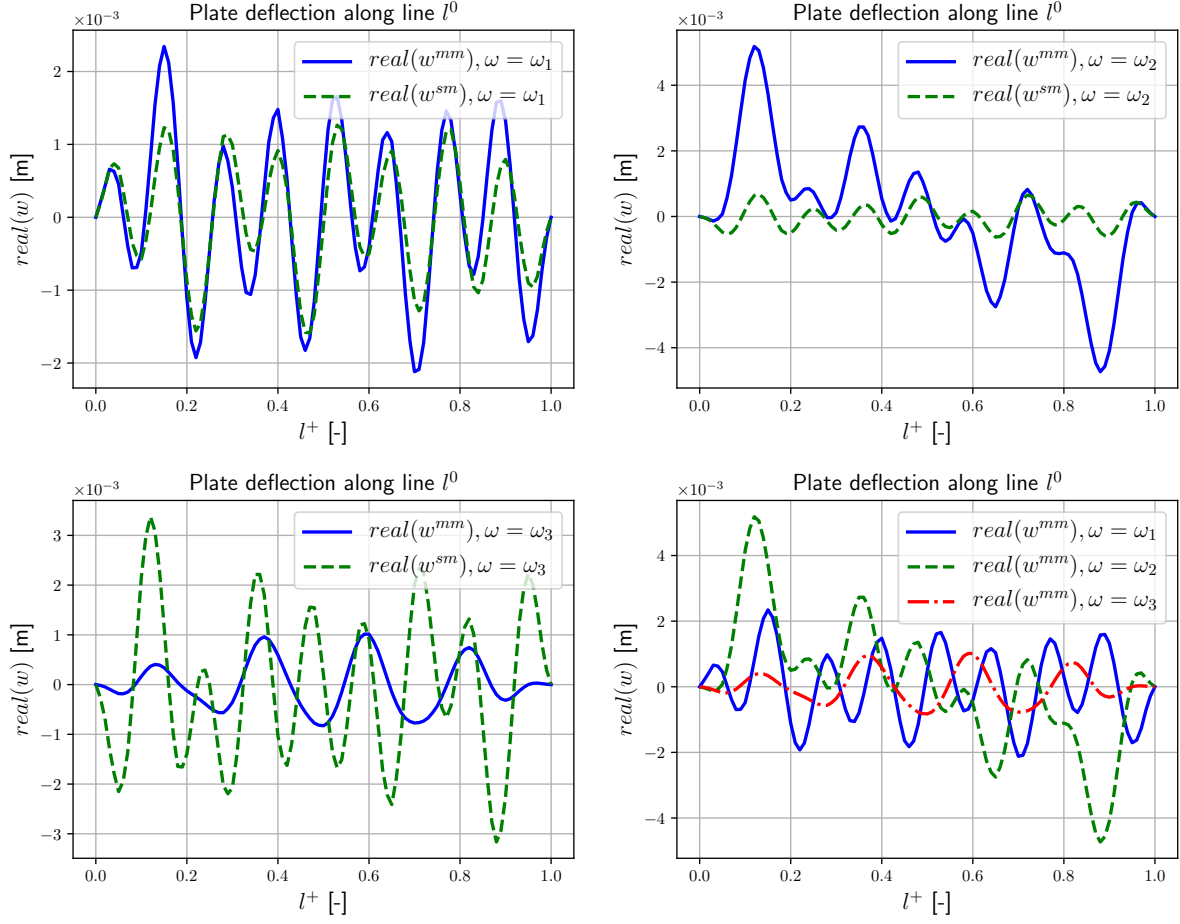


Figure 12: Comparison of the plate deflections calculated by the standard (sm) and the metamaterial (mm) models. The real parts of the plate deflection are plotted along line l^0 for frequencies $\omega_1 = 33000$ Hz, $\omega_2 = 35900$ Hz and $\omega_3 = 36200$ Hz.

In the plate equation (20), the unfolded inertia terms at the l.h.s. converge, as follows

$$\begin{aligned}
& \omega^2 \int_{\Gamma_0} \int_{\Xi_S} \mathcal{T}_\varepsilon(\rho^\varepsilon) \mathcal{T}_\varepsilon(\mathbf{u}^\varepsilon) \cdot \mathcal{T}_\varepsilon(\mathbf{v}^\varepsilon) + \omega^2 \frac{h^2}{12} \int_{\Gamma_0} \int_{\Xi_S} \mathcal{T}_\varepsilon(\rho^\varepsilon) \mathcal{T}_\varepsilon(\boldsymbol{\theta}^\varepsilon) \cdot \mathcal{T}_\varepsilon(\boldsymbol{\psi}^\varepsilon) \\
& \rightarrow -\omega^2 \int_{\Gamma_0} \rho_S \left((\mathbf{u}^0 + \chi_c \hat{u}_3) \cdot (\mathbf{v}^0 + \chi_c \hat{v}_3) + \frac{h^2}{12} (\boldsymbol{\theta}^0 + \chi_c \hat{\boldsymbol{\theta}}) \cdot (\boldsymbol{\psi}^0 + \chi_c \hat{\boldsymbol{\psi}}) \right), \tag{A.4}
\end{aligned}$$

where $\rho_S(y') = \chi_m(y')\rho_m + \chi_c(y')\rho_c$ is the solid density. Then we obtain the limit of the

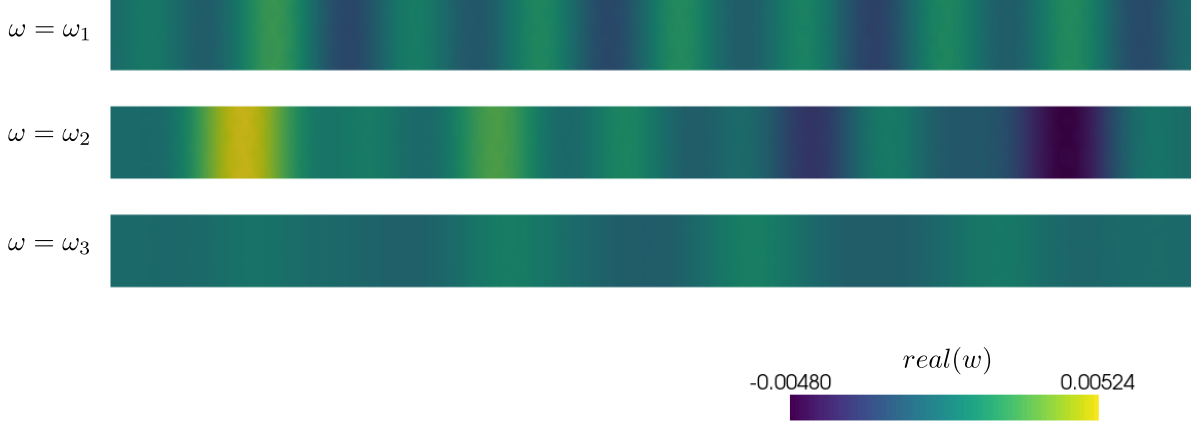


Figure 13: The distribution of the plate deflection (real part of w^{mm}) in the macroscopic domain Γ_0 .

unfolded elasticity terms with substituted heterogeneity anstaz (24),

$$\begin{aligned}
& - \int_{\Gamma_0} \int_{\Xi_S} [\mathcal{T}_\varepsilon(\mathbb{E}^\varepsilon) \bar{\nabla}^S \mathcal{T}_\varepsilon(\bar{\mathbf{u}}^\varepsilon)] : \mathcal{T}_\varepsilon(\bar{\nabla}^S \bar{\mathbf{v}}^\varepsilon) - \frac{h^2}{12} \int_{\Gamma_0} \int_{\Xi_S} [\mathcal{T}_\varepsilon(\mathbb{E}^\varepsilon) \bar{\nabla}^S \mathcal{T}_\varepsilon(\boldsymbol{\theta}^\varepsilon)] : \mathcal{T}_\varepsilon(\bar{\nabla}^S \boldsymbol{\psi}^\varepsilon) \\
& - \int_{\Gamma_0} \int_{\Xi_S} [\mathcal{T}_\varepsilon(\mathbf{S}^\varepsilon)(\mathcal{T}_\varepsilon(\bar{\nabla} u_3^\varepsilon) - (\mathcal{T}_\varepsilon(\boldsymbol{\theta}^\varepsilon)))] \cdot (\mathcal{T}_\varepsilon(\bar{\nabla} v_3^\varepsilon) - \mathcal{T}_\varepsilon(\boldsymbol{\psi}^\varepsilon)) \\
\rightarrow & + \int_{\Gamma_0} \left(\int_{\Xi_m} [\mathbb{E}_m(\bar{\nabla}_x^S \bar{\mathbf{u}}^0 + \bar{\nabla}_y^S \bar{\mathbf{u}}^1)] : (\bar{\nabla}_x^S \bar{\mathbf{v}}^0 + \bar{\nabla}_y^S \bar{\mathbf{v}}^1) + \int_{\Xi_c} [\mathbb{E}_c \bar{\nabla}_y^S \hat{\mathbf{u}}] : \hat{\mathbf{v}} \right) \\
& + \int_{\Gamma_0} \left(\int_{\Xi_m} [\mathbf{S}_m(\bar{\nabla}_x u_3^0 + \bar{\nabla}_y u_3^1 - \boldsymbol{\theta}^0)] \cdot (\bar{\nabla}_x v_3^0 + \bar{\nabla}_y v_3^1 - \boldsymbol{\psi}^0) + \int_{\Xi_c} [\mathbf{S}_c \bar{\nabla}_y \hat{u}_3] \cdot \bar{\nabla}_y \hat{v}_3 \right) \\
& + \frac{h^2}{12} \int_{\Gamma_0} \left(\int_{\Xi_m} [\mathbb{E}_m(\bar{\nabla}_x^S \boldsymbol{\theta}^0 + \bar{\nabla}_y^S \boldsymbol{\theta}^1)] : (\bar{\nabla}_x^S \boldsymbol{\psi}^0 + \bar{\nabla}_y^S \boldsymbol{\psi}^1) + \int_{\Xi_c} [\mathbb{E}_c \bar{\nabla}_y^S \hat{\boldsymbol{\theta}}] : \bar{\nabla}_y^S \hat{\boldsymbol{\psi}} \right) \\
= & \int_{\Gamma_0} \left(\mathcal{P}_m((\mathbf{u}^0, \mathbf{u}^1, \boldsymbol{\theta}^0, \boldsymbol{\theta}^1), (\mathbf{v}^0, \mathbf{v}^1, \boldsymbol{\psi}^0, \boldsymbol{\psi}^1)) + \mathcal{P}_c((\hat{\mathbf{u}}, \hat{\boldsymbol{\theta}}), (\hat{\mathbf{v}}, \hat{\boldsymbol{\psi}})) \right) .
\end{aligned} \tag{A.5}$$

The unfolded r.h.s. term in (20)

$$\begin{aligned}
& \frac{i\omega\rho_0}{\varepsilon\bar{h}} \int_{\Gamma_0} \int_{\Xi_S} (v_3^0 + \varepsilon v_3^1 + \chi_c \hat{v}_3) \varepsilon \llbracket p^1 \rrbracket_h^\pm \\
& + \frac{i\omega\rho_0}{\varepsilon} \int_{\Gamma_0} \int_{\partial\Xi_S} \int_{-1/2}^{1/2} \bar{\mathbf{n}} \cdot \left(\bar{\mathbf{v}}^0 + \varepsilon \bar{\mathbf{v}}^1 + \chi_c \hat{\mathbf{v}} - \varepsilon \bar{h} \zeta (\boldsymbol{\psi}^0 + \varepsilon \boldsymbol{\psi}^1 + \chi_c \hat{\boldsymbol{\psi}}) \right) (p^0 + \varepsilon p^1) ,
\end{aligned} \tag{A.6}$$

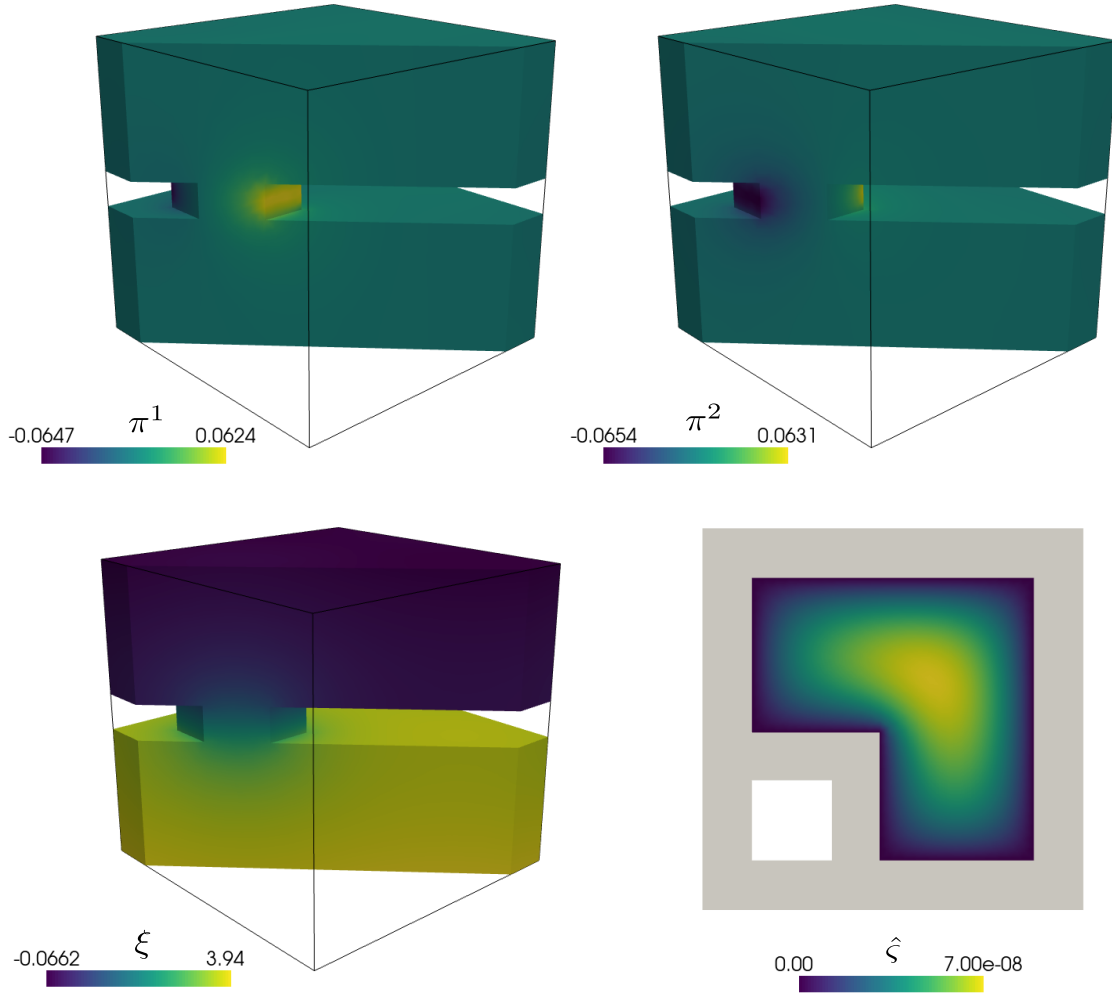


Figure 14: The characteristic responses of the local problems (33) and (34): top – Eq.(33), correctors π^β ($\hat{w}^\beta = 0$), bottom – Eq.(34), correctors $\xi, \hat{\xi}$.

converges to the limit expression

$$\begin{aligned}
 & \frac{i\omega\rho_0}{\hbar} \int_{\Gamma_0} \left(v_3^0 \int_{\Xi_S} \llbracket p^1 \rrbracket_{\hbar}^{\pm} + \int_{\Xi_c} \hat{v}_3 \llbracket p^1 \rrbracket_{\hbar}^{\pm} \right) \\
 & + i\omega\rho_0 \int_{\Gamma_0} \left(\bar{v}^0 \cdot \int_{-1/2}^{1/2} \int_{\partial\Xi_S} \bar{\mathbf{n}} p^1 + p^0 \int_{\partial\Xi_S} \bar{v}^1 \cdot \bar{\mathbf{n}} \right).
 \end{aligned} \tag{A.7}$$

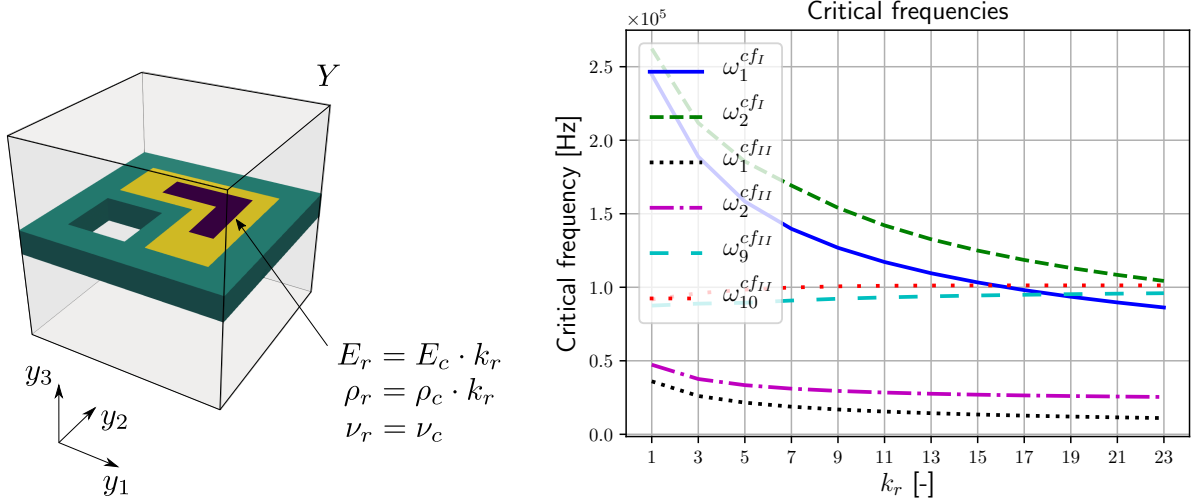


Figure 15: Left: the microscopic geometry with the resonator embedded in the elastic inclusion. Right: the dependence of the critical frequencies ω^{cfI} and ω^{cfII} on the material properties of the resonator part which are parametrized by k_r .

Appendix B. Properties of the homogenized coefficients

Appendix B.1. Proof of the homogenized coefficients symmetry relationship

We prove the symmetry relationships claimed in Proposition 2, assertion (i). The following symmetry holds $M_{3\alpha} = M_{\alpha 3}$,

$$\begin{aligned} M_{3\alpha} &= \frac{\rho_0}{\bar{h}} \langle \langle \mathcal{T}_{i\omega}(\hat{\omega}^3, \eta^3), (-\hat{\omega}^\alpha, \eta^\alpha) \rangle \rangle_c = \frac{\rho_0}{\bar{h}} \langle \langle \mathcal{T}_{i\omega}(\hat{\omega}^\alpha, \eta^\alpha), (-\hat{\omega}^3, \eta^3) \rangle \rangle_c \\ &= -\rho_0 \int_{\partial \Xi_S} n_\alpha \int_{-1/2}^{1/2} \eta^3 = M_{\alpha 3}. \end{aligned} \quad (\text{B.1})$$

The symmetry $M_{\alpha\beta} = M_{\beta\alpha}$, α, β is straightforward,

$$M_{\alpha\beta} = \langle \langle \mathcal{T}_{i\omega}(\hat{\omega}^\alpha, \eta^\alpha), (\hat{\omega}^\beta, \eta^\beta) \rangle \rangle_c = M_{\beta\alpha}. \quad (\text{B.2})$$

Further, $C_\alpha = 0$ by some symmetry arguments. Symmetry of $D_{3\alpha} = D_{\alpha 3}^*$ and $D_{\alpha\beta}^* = D_{\beta\alpha}$ is obtained using the autonomous local problems. Due to (56), we get

$$\begin{aligned} D_{\alpha\beta}^* &= \int_{Y^*} \partial_\alpha^y \eta^\beta = \langle \langle \mathcal{T}_{i\omega}(\hat{w}^\alpha, \pi^\alpha), (\hat{\omega}^\beta, -\eta^\beta) \rangle \rangle_c \\ &= \langle \langle \mathcal{T}_{i\omega}(\hat{\omega}^\beta, \eta^\beta), (\hat{w}^\alpha, -\pi^\alpha) \rangle \rangle_c = \bar{h} \int_{\partial \Xi_S} n_\beta \int_{-1/2}^{1/2} \pi^\alpha d\zeta = D_{\beta\alpha}. \\ D_{\alpha 3}^* &= \int_{Y^*} \partial_\alpha^y \eta^3 = \langle \langle \mathcal{T}_{i\omega}(\hat{w}^\alpha, \pi^\alpha), (\hat{\omega}^3, -\eta^3) \rangle \rangle_c = \langle \langle \mathcal{T}_{i\omega}(\hat{\omega}^3, \eta^3), (\hat{w}^\alpha, -\pi^\alpha) \rangle \rangle_c \\ &= -i\omega \frac{\bar{h}}{\rho^0} \int_{\Xi_c} \rho \hat{w}^\alpha + \int_{\Xi_S} [\pi^\alpha]_{\bar{h}}^\pm \cdot 1 = D_{3\alpha}. \end{aligned} \quad (\text{B.3})$$

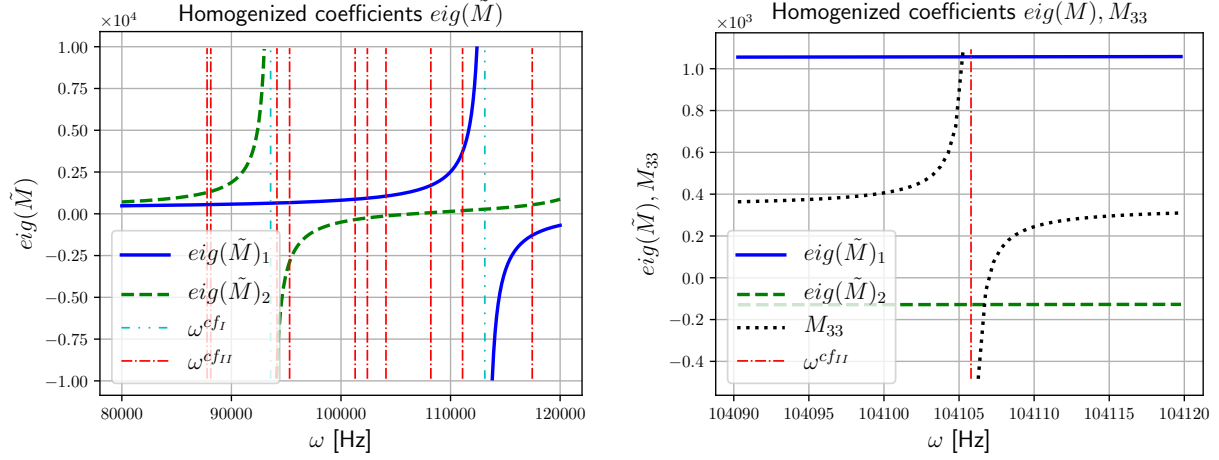


Figure 16: Left: the eigenvalues of homogenized coefficients \tilde{M} . Right: the eigenvalues of \tilde{M} and coefficient M_{33} around a resonant frequency.

Symmetries declared in $(67)_{2,3}$ can be proved easily using the local problems (33)-(36). Coefficient F can be expressed using (34) (with $q = \xi$), as follows:

$$\begin{aligned}
 F &= - \int_{I_y^+} \xi + \int_{I_y^-} \xi = \langle \langle \mathcal{T}_{i\omega}(\hat{\varsigma}, \xi), (\hat{\varsigma}, \xi) \rangle \rangle_c \\
 &= \frac{\bar{h}}{\rho_0} \left[\hat{b}_c(\hat{\varsigma}, \hat{\varsigma}) - \omega^2 \int_{\Xi_c} \rho \hat{\varsigma} \cdot \hat{\varsigma} \right] + \int_{Y^*} \nabla_y \xi \cdot \nabla_y \xi,
 \end{aligned} \tag{B.4}$$

if we chose the test function $\hat{v} = \hat{\varsigma}$ in (34).

The symmetry can be proved, $C'_k = C_k = 0$, $k = 1, \dots, 3$. Firstly,

$$\begin{aligned}
 C'_\alpha &= \int_{I_y^+} \eta^\alpha - \int_{I_y^-} \eta^\alpha = \langle \langle \mathcal{T}_{i\omega}(\hat{\varsigma}, \xi), (\hat{\omega}^\alpha, -\eta^\alpha) \rangle \rangle_c \\
 &= \langle \langle \mathcal{T}_{i\omega}(\hat{\omega}^\alpha, \eta^\alpha), (\hat{\varsigma}, -\xi) \rangle \rangle_c = \bar{h} \int_{\partial \Xi_S} n_\alpha \int_{-1/2}^{1/2} \xi(\cdot, \zeta) d\zeta = C_\alpha.
 \end{aligned} \tag{B.5}$$

In analogy (note $\int_{\Xi_S} [\hat{\xi}]_h^\pm = 0$ due to the special shape on the holes, but $C'_3 \neq 0$ in general.)

$$\begin{aligned}
 C'_3 &= \int_{I_y^+} \eta^3 - \int_{I_y^-} \eta^3 = \langle \langle \mathcal{T}_{i\omega}(\hat{\varsigma}, \xi), (\hat{\omega}^3, -\eta^3) \rangle \rangle_c \\
 &= \langle \langle \mathcal{T}_{i\omega}(\hat{\omega}^3, \eta^3), (\hat{\varsigma}, -\xi) \rangle \rangle_c = -i\omega \frac{\bar{h}}{\rho_0} \int_{\Xi_c} \rho \hat{\varsigma} + \int_{\Xi_S} [\hat{\xi}]_h^\pm \cdot 1 = C_3.
 \end{aligned} \tag{B.6}$$

Appendix C. Homogenized coefficients – computation using the discretized micro-problem

Here we derive formulae for computing the homogenized coefficients reported in Section 5.1.3. We disregard the assumption of the z -symmetric cells Y , such that the cancellations declared in Proposition 2 (iii) may not apply, in general.

- [1] E. L. Yedeg, E. Wadbro, P. Hansbo, M. G. Larson, M. Berggren, A nitsche-type method for helmholtz equation with an embedded acoustically permeable interface, *Comput. Method. Appl. M.* 304 (2016) 479–500. doi:10.1016/j.cma.2016.02.032.
- [2] A. Bonnet-Bendhia, D. Drissi, N. Gmati, Mathematical analysis of the acoustic diffraction by a muffler containing perforated ducts, *Math. Models and Methods in Appl. Sci.* 15 (7) (2005) 1059–1090. doi:10.1142/s0218202505000649.
- [3] B. Schweizer, Effective Helmholtz problem in a domain with a Neumann sieve perforation, *J. Math. Pure. Appl.* 142 (2020) 1–22. doi:10.1016/j.matpur.2020.08.002.
- [4] B. Delourme, H. Haddar, P. Joly, Approximate models for wave propagation across thin periodic interfaces, *J. Math. Pure. Appl.* 98 (1) (2012) 28–71. doi:10.1016/j.matpur.2012.01.003.
- [5] X. Claeys, B. Delourme, High order asymptotics for wave propagation across thin periodic interfaces, *Asymptotic Anal.* 83 (1-2) (2013) 35–82. doi:10.3233/asy-2012-1150.
- [6] J.-J. Marigo, A. Maurel, Homogenization models for thin rigid structured surfaces and films, *J. Acoust. Soc. Am.* 140 (1) (2016) 260–273. doi:10.1121/1.4954756.
- [7] J.-J. Marigo, A. Maurel, Two-scale homogenization to determine effective parameters of thin metallic-structured films, *P. Roy. Soc. Lond. A. Mat.* 472 (2192) (2016). doi:10.1098/rspa.2016.0068.
- [8] E. Rohan, V. Lukeš, Homogenization of the acoustic transmission through perforated layer, *J. Comput. Appl. Math.* 234 (2010) 1876–1885.
- [9] E. Rohan, V. Lukeš, Homogenization of the vibro-acoustic transmission on perforated plates, *Appl. Math. Comput.* 361 (2019) 821–845. doi:doi.org/10.1016/j.amc.2019.06.005.
- [10] B. Liang, J. Cheng, C. Qiu, Wavefront manipulation by acoustic metasurfaces: from physics and applications, *Nanophoto.* 7 (6) (2018) 1191–1205. doi:10.1515/nanoph-2017-0122.
- [11] H. Zou, P. Li, P. Peng, An ultra-thin acoustic metasurface with multiply resonant units, *Phys. Lett. A* 384 (7) (2020) 126151. doi:10.1016/j.physleta.2019.126151.
- [12] S. Liang, T. Liu, H. Gao, Z. Gu, S. An, J. Zhu, Acoustic metasurface by layered concentric structures, *Phys. Rev. Research* 2 (Dec 2020). doi:10.1103/PhysRevResearch.2.043362.
- [13] R. Hu, C. Oskay, Spectral variational multiscale model for transient dynamics of phononic crystals and acoustic metamaterials, *Comput. Method. Appl. M.* 359 (2020) 112761. doi:10.1016/j.cma.2019.112761.

- [14] G. Ma, M. Yang, S. Xiao, et al., Acoustic metasurface with hybrid resonances, *Nature Mater.* 13 (2014) 873–878. doi:doi.org/10.1038/nmat3994.
- [15] K. Miyata, Y. Noguchi, T. Yamada, K. Izui, S. Nishiwaki, Optimum design of a multi-functional acoustic metasurface using topology optimization based on zwicker’s loudness model, *Comput. Method. Appl. M.* 331 (2018) 116–137. doi:doi:10.1016/j.cma.2017.11.017.
- [16] Y. Noguchi, T. Yamada, K. Izui, S. Nishiwaki, Topology optimization for hyperbolic acoustic metamaterials using a high-frequency homogenization method, *Comput. Method. Appl. M.* 335 (2018) 419–471. doi:10.1016/j.cma.2018.02.031.
- [17] Y. Fu, C. Shen, Y. Cao, et al., Reversal of transmission and reflection based on acoustic metagratings with integer parity design, *Nat. Commun.* 10 (1) (2019). doi:10.1038/s41467-019-10377-9.
- [18] S. Huang, X. Fang, X. Wang, B. Assouar, Q. Cheng, Y. Li, Acoustic perfect absorbers via helmholtz resonators with embedded apertures, *J. Acoust. Soc. Am.* 145 (1) (2019) 254–262. doi:10.1121/1.5087128.
- [19] R. Pernas-Salomón, G. Shmuel, Dynamic homogenization of composite and locally resonant flexural systems, *J. Mech. Phys. Solids* 119 (2018) 43–59. doi:10.1016/j.jmps.2018.06.011.
- [20] G. Milton, J. Willis, On modifications of newton’s second law and linear continuum elastodynamics, *Proc. R. Soc. A* 483 (2007) 855–880. doi:10.1098/rspa.2006.1795.
- [21] Y. Liu, Z. Liang, J. Zhu, L. Xia, O. Mondain-Monval, T. Brunet, A. Alù, J. Li, Willis metamaterial on a structured beam, *Phys. Rev. X* 9 (2019). doi:10.1103/PhysRevX.9.011040.
- [22] G. Milton, M. Briane, J. Willis, On cloaking for elasticity and physical equations with a transformation invariant form, *New J. Phys.* 8 (10) (2006) 248–248. doi:10.1088/1367-2630/8/10/248.
- [23] A. Madeo, P. Neff, I. Ghiba, L. Placidi, G. Rosi, Wave propagation in relaxed micromorphic continua: modeling metamaterials with frequency band-gaps, *Continuum Mech. Thermodyn.* 27 (4-5) (2015) 551–570. doi:10.1007/s00161-013-0329-2.
- [24] J. Auriault, G. Bonnet, Dynamique des composites elastiques periodiques, *Arch. Mech.* 37 (1985) 269–284.
- [25] A. Ávila, G. Griso, B. Miara, E. Rohan, Multiscale modeling of elastic waves: Theoretical justification and numerical simulation of band gaps, *Multiscale Model. Sim.* 7 (2008) 1–21. doi:10.1137/060677689.

- [26] V. P. Smyshlyaev, Propagation and localization of elastic waves in highly anisotropic periodic composites via two-scale homogenization, *Mech. Mater.* 41 (2009) 434–447. doi:10.1016/j.mechmat.2009.01.009.
- [27] E. Rohan, B. Miara, F. Seifrt, Numerical simulation of acoustic band gaps in homogenized elastic composites, *Int. J. Eng. Sci.* 47 (4) (2009) 573–594. doi:10.1016/j.ijengsci.2008.12.003.
- [28] J. Vondřejc, E. Rohan, J. Heczko, Shape optimization of phononic band gap structures using the homogenization approach, *Int. J. Solids Struct.* 113-114 (2017) 147–168. doi:10.1016/j.ijsolstr.2017.01.038.
- [29] E. Rohan, B. Miara, Elastodynamics of strongly heterogeneous periodic plates using Reissner-Mindlin and Kirchhoff-Love models, *Zamm-z. Angew. Math. Me.* 96 (3) (2016) 304–326. doi:10.1002/zamm.201400145.
- [30] E. Rohan, R. Cimrman, B. Miara, Modelling response of phononic Reissner-Mindlin plates using a spectral decomposition, *Appl. Math. Comput.* 258 (2015) 617–630. doi:10.1016/j.amc.2014.12.037.
- [31] E. Gurvich, J. Webster, Weak solutions for a poro-elastic plate system (2021). arXiv:2103.07569.
- [32] A. Cioranescu, D. Damlamian, G. Griso, D. Onofrei, The periodic unfolding method for perforated domains and neumann sieve models, *J. Math. Pure. Appl.* 89 (3) (2008) 248–277. doi:10.1016/j.matpur.2007.12.008.
- [33] R. Cimrman, V. Lukeš, E. Rohan, Multiscale finite element calculations in python using sfepy, *Adv. Comput. Math.* 45 (4) (2019) 1897–1921. doi:10.1007/s10444-019-09666-0.
- [34] E. Rohan, V. Lukeš, Sensitivity analysis for optimal design of perforated plates in vibro-acoustics: homogenization approach, in: *Proceedings of ISMA 2012 – USD 2012*, KU Leuven, 2012, pp. 4201–4214.
- [35] E. Rohan, V. Lukeš, Homogenized perforated interface in acoustic wave propagation – modeling and optimization, in: Z. D. et.al. (Ed.), *Proc. of the 11th International Conference on Vibration Problems, ICOVP 2013*, Lisbon, Portugal, 2013, pp. 1–10.
- [36] Y. Noguchi, T. Yamada, Topology optimization of acoustic metasurfaces by using a two-scale homogenization method (2020). arXiv:2010.10844.
- [37] G. Maierhofer, N. Peake, Wave scattering by an infinite cascade of non-overlapping blades, *J. Sound Vib.* 481 (2020) 115418. doi:10.1016/j.jsv.2020.115418.

- [38] A. Marciniak-Czochra, A. Mikelic, A Rigorous Derivation of the Equations for the Clamped Biot-Kirchhoff-Love Poroelastic plate, *Arch. Ration. Mech. An.* 215 (2015) 1035–1062. doi:10.1007/s00205-014-0805-2.
- [39] L. Bociu, S. Čanić, B. Muha, J. Webster, Multilayered poroelasticity interacting with Stokes flow (2020). arXiv:2011.12602.